Since January 2020 Elsevier has created a COVID-19 resource centre with free information in English and Mandarin on the novel coronavirus COVID-19. The COVID-19 resource centre is hosted on Elsevier Connect, the company's public news and information website.

Separation and Purification Technology 298 (2022) 121565

Contents lists available at ScienceDirect

Separation and Purification Technology

journal homepage: www.elsevier.com/locate/seppur

Electrospun nanofibrous membrane with antibacterial and antiviral properties decorated with Myoporum bontioides extract and silver-doped carbon nitride nanoparticles for medical masks application

Pinhong Chen [a,b], Zhi Yang [a], Zhuoxian Mai [a,b], Ziyun Huang [a,b], Yongshuang Bian [a,b], Shangjing Wu [a,b], Xianming Dong [a,b], Xianjun Fu [c], Frank Ko [d], Shiying Zhang [e], Wenxu Zheng [a,b], Shengsen Zhang [a,*], Wuyi Zhou [a,b,*]

[a] Key Laboratory of the Ministry of Bio-based Materials and Energy Education, South China Agricultural University, Guangzhou 510642, China
[b] Research Center of Biomass 3D Printing Materials, College of Materials and Energy, South China Agricultural University, Guangzhou 510642, China
[c] Marine Traditional Chinese Medicine Research Center, Qingdao Academy of Traditional Chinese Medicine, Shandong University of Traditional Chinese Medicine, Qingdao 266114, China
[d] Department of Materials Engineering, The University of British Columbia, Vancouver, BC V6T 1Z4, Canada
[e] Hunan Key Laboratory of Applied Environmental Photocatalysis, Changsha University, Changsha 410022, China

ARTICLE INFO

Keywords:
Personal protective equipment (PPE)
Myoporum bontioides
Silver-doped carbon nitride
Nanofibrous membrane
Photocatalytic antibacterial and antiviral
Molecular docking

ABSTRACT

Public health safety issues have been plaguing the world since the pandemic outbreak of coronavirus disease (COVID-19). However, most personal protective equipments (PPE) do not have antibacterial and anti- toxicity effects. In this work, we designed and prepared a reusable, antibacterial and anti-toxicity Polyacrylonitrile (PAN) based nanofibrous membrane cooperated with Ag/g-C_3N_4 (Ag-CN), Myoporum.bontioides (*M. bontioides*) plant extracts and Ag nanoparticles (NPs) by an electrospinning-process. The SEM and TEM characterization revealed the formation of raised, creased or wrinkled areas on the fiber surface caused by the Ag nanoparticles, the rough surface prevented the aerosol particles on the fiber surface from sliding and stagnating, thus providing excellent filtration performance. The PAN/*M. bontioides*/Ag-CN/Ag nanofibrous membrane could be employed as a photocatalytic bactericidal material, which not only degraded 96.37% of methylene blue within 150 min, but also exhibited the superior bactericidal effect of 98.65 ± 1.49% and 97.8 ± 1.27% against *E. coli* and *S. aureus*, respectively, under 3 hs of light exposure. After 3 cycles of sterilization experiments, the PAN/*M. bontioides*/Ag-CN/Ag nanofibrous membrane maintained an efficient sterilization effect. Molecular docking revealed that the compounds in *M. bontioides* extracts interacted with neo-coronavirus targets mainly on Mpro and RdRp proteins, and these compounds had the strongest docking energy with Mpro protein, the shortest docking radius, and more binding sites for key amino acids around the viral protein targets, which influenced the replication and transcription process of neo-coronavirus. The PAN/*M.bontioides*/Ag-CN/Ag nanofibrous membrane also performed significant inhibition of influenza A virus H3N2. The novel nanofiber membrane is expected to be applied to medical masks, which will improve human isolation and protection against viruses.

1. Introduction

Public health safety has been plagued by the 2019 global coronavirus disease (COVID-19) pandemic caused by Severe Acute Respiratory Syndrome Coronavirus-2 (SARS-CoV-2). Most coronaviruses and influenza viruses are transmitted from infected to uninfected individuals through tiny droplets in the air exhaled during coughing and sneezing or in oral secretions [1,2]. Personal protective equipment (PPE) [3,4], which is currently widely promoted for use, provides effective protection for individuals [2,5-7]. Since the viability *in vitro* of SARS-CoV-2 has a prolonged duration, the pathogens intercepted and captured at the surface of PPE still have persistent infectious activity, which can be susceptible to cross-infection and virus transmission [8-12]. Therefore, it is further in need of a protective masks with efficient filtration properties to prevent the entry of viruses, while killing them effectively and rapidly.

* Corresponding authors.
E-mail address: zhouwuyi@scau.edu.cn (W. Zhou).

https://doi.org/10.1016/j.seppur.2022.121565
Received 1 May 2022; Received in revised form 3 June 2022; Accepted 20 June 2022
Available online 24 June 2022

The nanofibrous membranes prepared by electrospinning technology have been subjected to wide studies in air filtration [2,3,5,13-19]. The nanofibrous membranes with micro-and nano-diameters, high porosity, and large surface area to volume ratio can dramatically intercept micro- and nano-particles, which promotes high filtration efficiency and low-pressure drop [14,20-23]. Meanwhile, the nanofibrous membrane surface will carry electrostatic ions, which is able to attract airborne pathogens and particles during the filtration process, reducing the risk of diseases [24-29]. Polyacrylonitrile (PAN) is a typical polar polymer that is frequently employed as a filter membrane for respirators, offering good filtration performance and recyclability, and effective isolation of airborne bacteria and viruses [30-32], as well as it has low toxicity and good biocompatibility [33-35]. Consequently, it is one of the ideal materials for new medical masks in the future.

So far, there are few effective drugs that are available for SARS-CoV-2, where the safety of the new emerging drugs still remained to be verified. Doctors successfully worked with Chinese herbs to help patients with mild symptoms improve their constitution to overcome the virus, which was prevalent in China at the time. Subsequently various herbs (baicalin, Panax notoginseng, and licorice roots [6,27,36], etc.) were found to be effective against coronavirus. Among them, Myoporum bontioides (*M.bontioides*) was a traditional folk medicine whose main components were terpenoids and their derivatives, flavonoids and trace metal elements (Fig. S1) [37-40]. The terpenoids and flavonoids of *M. bontioides* were found to have antibacterial effects against a variety of bacteriasm, as effective as inhibitory abilities against various viruses [37-40]. For instance, the essential oil of the fresh leaves of *M.bontioides* showed 80% antiviral activity against herpes simplex virus type I (HSV-I) [41]. In test tube experiments, the antiproliferative or cytotoxic activity of the compound epingaione at a concentration of 50 pg/mL was 79.24% and 50.83% against human SH-SY5Y neuroblastoma and TE-671 sarcoma cells [42]. It is probably due to the important role played by terpenoids and flavonoids contained in *M.bontioides*.

Silver is considered one of the most important elements because of its excellent antibacterial properties and relatively reasonable cytotoxic levels [43,44]. Alternatively, polymer hybrid materials embedded with silver nanoparticles have received considerable attention for their superior properties (photovoltaic, catalytic). When applied in reasonable dosages, Ag nanoparticles (NPs) are regarded as safe and effective topical antimicrobial agents for the skin wound dressing [34,45]. Some studies have found that surface modification of electrospun nanofibers with nanoparticles is a simple and effective way to build structures on the surface. The rough surface formed by projections, creases or wrinkled areas allows aerosol particles on the fiber surface to not slide and stagnate, thus enabling excellent filtration performance [46,47]. AgNPs are applied to commercial air filters to improve resistance to MS2 and H1N1 viruses [46,48]. Researches have proven that the utilization of AgNPs in air filtration against viruses is feasible [48,49]. However, more research on related nanofiber membranes is still needed.

Currently, one of the effective methods is the addition of nano-photocatalysts into the protective mats, which can effectively kill surrounding pathogens and reduce their adhesion [50-52]. The mechanism of its inhibitory activity is demonstrated by inducing the release of reactive oxygen species (ROS), disrupting protein function and DNA, as well as damaging bacterial cell membranes [53,54]. The typical photocatalysts include TiO_2 [22,55], ZnO [16], Bi_2WO_6 [56] and g-C_3N_4. Among them, the graphitic carbon nitride (g-C_3N_4) is a non-toxic and chemically stable non-metallic polymeric photocatalyst with a narrow bandgap of 2.7 eV that can degrade environmental pollutants when driven by visible light [57]. g-C_3N_4 is remarkable in photocatalytic degradation and photocatalytic hydrogen production. However, the catalytic efficiency of a single g-C_3N_4 is low, so it is usually combined with metals, such as the well-known Ag, Pt and Au [58,59]. Noble metal nanoparticles can act as active sites and play an important role in effective visible light absorption and subsequent photocatalytic reactions [60]. The possible reason is that noble metal nanoparticles can strongly absorb visible light because their localized surface plasmon resonance can be tuned by changing their size, shape and surroundings. Hence, by adding photocatalysts to the protective material to self-clean in the presence of light is an essential modification for the reusability of the protective material [53].

In this study, we present a functional approach for the fabrication of multifunctional membranes for protective mats modification by a direct electrospinning of membrane decorated with Ag/g-C_3N_4 (Ag-CN) and AgNPs together (Fig. 1). The manufacturing was accomplished in one step by electrospinning of PAN solution containing Ag-CN and Ag nanoparticles. The nanofibrous membrane structure was investigated, as well as the particle filtration performance. *E. coli* and *S. aureus* were employed to evaluate the antibacterial properties of the novel nanofibrous membrane. The antiviral properties of the nanofibrous membrane were evaluated with influenza A virus H3N2. We believe that this electrospun nanofibous membranes might own antiviral, antibacterial and efficient filtration properties, which is important for capturing air pollutants and preventing infection and transmission of respiratory infectious diseases. It will be promising for application in medical protective materials.

2. Experimental section

2.1. Materials

Polyacrylonitrile (PAN, Mw = 150,000 g/mol) was purchased from Pingjiang Chemical Reagent Co., Ltd. (Guangdong, China), N, N-Dimethylformamide (DMF, AR) was brought from Tianjin Yongda Chemical Reagent Co., Ltd. (Tianjin,China), $AgNO_3$ (AR) was obtained from Tianjin Qilun Chemical Technology Co.,Ltd.(Tianjin,China), Melamine (AR) was purchased from Aladdin, Anhydrous ethanol (AR) was gotten from Tianjin Damao Chemical Reagent Factory.

2.2. Synthesis of Ag-CN nanoparticles

The metal-free g-C_3N_4 powder was synthesized by heating melamine in a muffle furnace. 1 g g-C_3N_4 was added to 100 mL of deionized water, the suspension was mixed for 30 min, and sonicated for 30 min. Subsequently, 3 wt% $AgNO_3$ was rapidly added to the above suspension, whereupon the suspension was irradiated under a xenon lamp and magnetically stirred for 2 h. The suspension was filtered, washed with deionized water, and dried at 80 °C for 12 h.

2.3. Extraction of M. bontioides

The fresh leaves of *M. bontioides* were picked fresh from the planting fields at the agricultural training base of South China Agricultural University and dried in a cool place for 7d, then dried at 45 °C for 8 h and crushed to obtain the powder. Then, the powder was cold soaked twice (14d, 7d) before with 60% ethanol solution, filtered, combined filtrate, distilled under reduced pressure (Rotary Evaporator RE-2000A, Shanghai Yarong Biochemical Instrument Factory) to obtain the infusion, which was kept at low temperature.

2.4. Fabrication of the PAN/M. bontioides/Ag-CN/Ag nanofibrous membrane

To prepare the PAN/*M. bontioides*/Ag-CN/Ag nanofibrous membrane, Ag-CN (1 wt%) was first dispersed in 10 mL of N, N-dimethylformamide (DMF) and after this, *M. bontioides* (3, 5, 7 wt%) mixture was added in a continuous sonication for 30 min to disperse the carbon nitride nanoparticles. After obtaining a homogeneous mixture, PAN (Mw = 150,000 g/mol, 8 wt%) was mixed with the solution using a magnetic stirrer (1000 rpm). The solution was kept under stirring for 1 h until the polymer was completely dissolved in DMF. Finally, different concentrations of silver nitrate (3, 5, 7 wt%) were added to the DMF

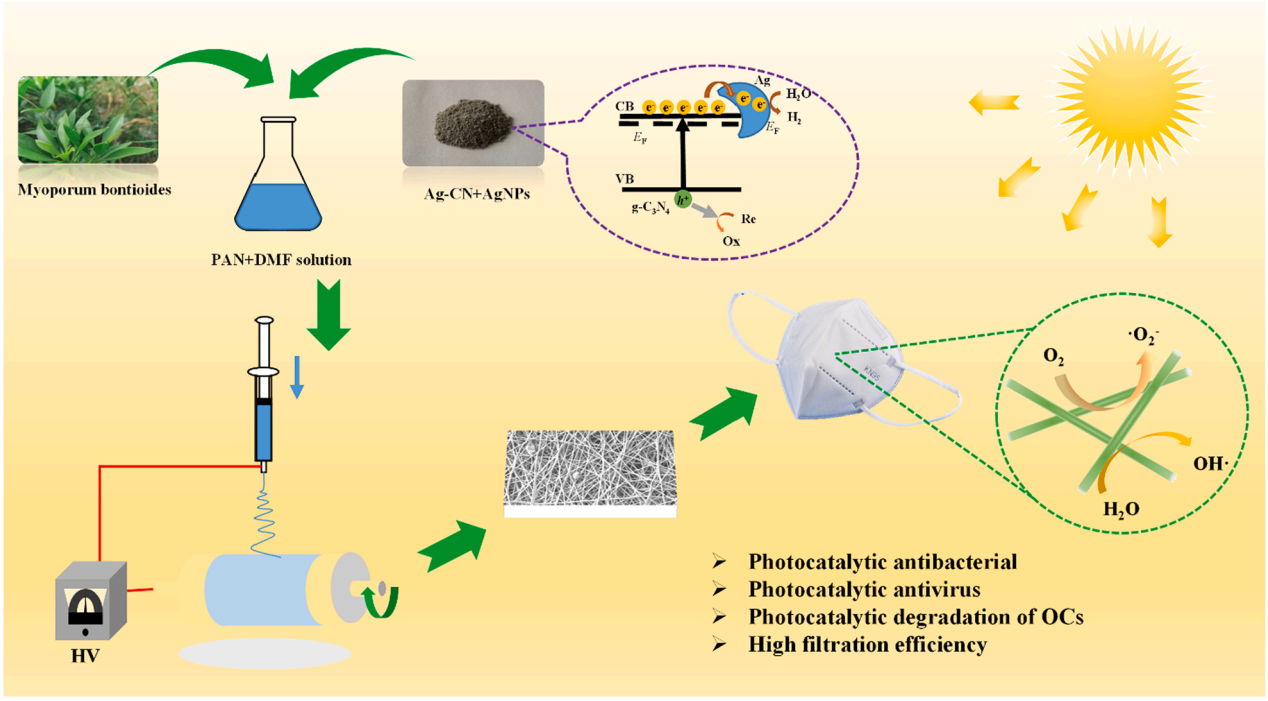

Fig. 1. Fabrication steps of the PAN/*M.bontioides*/Ag-CN/Ag nanofibrous membrane: wide source PAN, plant extracts of *M.bontioides*, Ag-CN and AgNPs are electrospun into a nano-network structure. The electrospun membranes are applied to the filter layer of the mask, because the nanofibrous membrane structure has excellent air ventilation and particle filtration efficiency; when the light hits the surface, Ag-CN utilizes the light energy to generate ROS, which revitalize the mask and kill the pathogens on the surface, making the mask recyclable.

solution. After that, the solution was kept overnight with stirring until its color turned to dark brown.

Fabrication of the PAN/*M. bontioides*/Ag-CN/Ag nanofibrous membrane was carried out by the electrospinning machine (TL-01, Shenzhen Tongli Micro-Nano Technology Co., Ltd.). The homogeneous solution was transferred to a 20 mL syringe that had an 18G metal needle. The distance from the needle to the collector was 13 cm, the applied voltage was 15 kV, the flow rate was 1 mL/h, and the electrospinning time was 1 h. The room temperature is maintained at 25 °C.

2.5. Characterization

The surface morphology of nanofibrous membrane was examined under a scanning electron microscope (SEM, ZEISS EVO MA 15). The diameter distributions of the nanofibers were determined by image J analysis using manometry on > 90 slices from SEM images. A transmission electron microscope (TEM, FEI/Talos L120C) was used to examine the surface morphology of the nanofibrous membrane. Wide-angle X-ray diffraction (XRD) analysis was performed using a Bruker D8 Advance (Cu Kα irradiated radiation) diffractometer to assess the physical state of the nanofibrous membrane. Fourier transform infrared spectroscopy (FT-IR) was employed to determine the structure and stability of the drug in the nanofibrous membrane by a Nicolet IS10 FTIR spectrometer (Thermo Fisher). Measured the viscosity of the nanofibrous membrane by a rotary viscometer (NDJ-5S, Shanghai Changji Geological Instruments Co., Ltd.). The conductivity of the nanofibrous membrane was monitored by a conductivity meter (DDS-11A, Shanghai INESA Scientific Instrument Co., Ltd.). Three different positions were conducted for each membrane and the average value was calculated.

2.6. Photocatalytic degradation and self-cleaning studies

The photocatalytic properties of the prepared the PAN/*M. bontioides*/Ag-CN/Ag nanofibrous membranes was investigated using methylene blue (MB) as a probe molecule. The 2 cm × 2 cm size nanofibrous membranes were placed in 100 mL of 10 mg/L MB solution and stirred for 150 min under a xenon lamp (PLS-SXE300D, Beijing Bofeilai Technology Co., Ltd.) with a light intensity of 75,000 lx. The absorbance of the purified solution at OD_{663} was recorded at 10 min intervals. The reduction rate was calculated by the following equation [53,61,62]:

$$Reduced\ \ rate(\%) = ln\frac{C_t}{C_0} \times 100\% \tag{1}$$

$$ln\frac{C_t}{C_0} = kt \tag{2}$$

where C_t represents OD_{663} after different illumination times, C_0 represents OD_{663} before illumination, and K is the first-order rate constant given by the slope of ln (C_0/C_t) versus t [53,61,62].

$$ln2 = kt_{1/2} \tag{3}$$

where $t_{1/2}$ is the time needed to reduce the initial concentration of the analyte to half of its initial concentration value.

2.7. Particulate filtration effifficiency (PFE) and pressure difference

The particulate filtration efficiency of the material was measured by filtering NaCl aerosols that simulate viral and bacterial filtration. An automated filter tester (Model 8130, TSI, Shoreview, Minnesota, MN. USA) was used to measure submicron particle filtration efficiency of the PAN/*M.bontioides*/Ag-CN/Ag nanofibrous membrane. NaCl particle loading experiments were also performed during the period, with a loading time of 1 min and a loading mass of 50 mg.

The submicron particulate filtration efficiency is defined as follows [2,15,16,21,63]:

PFE: The ratio of aerosol concentration captured by the mask to the original upstream aerogel concentration.

$$\text{Permeation efficiency } (\%) = (\text{aerosol concentration through the mask})/(\text{upstream aerosol concentration in the air}) \times 100\% \quad (4)$$

$$\text{Protection effifficiency } (\%) = 100 - \text{penetration effifficiency } (\%) \quad (5)$$

Inhalation resistance: the ventilation resistance generated by a certain airflow in the inhalation direction of the mask.

The quality factor (QF) could be calculated by the following Eq.6 [2,46,64].

$$QF = -\frac{ln(1-\eta)}{\Delta P} \quad (6)$$

where η and ΔP represented the filtration efficiency and pressure drop across the filter, respectively.

2.8. Antimicrobial activity assays

The antibacterial experiment of nanofibrous membranes was conducted by colony counting method. Gram-negative Escherichia coli (*E. coli*, OD_{600} = 0.33, 1OD = 1.0 × 10^9 cfu/mL) and Gram-positive Staphylococcus aureus (*S. aureus*, OD_{600} = 0.14, 1OD = 1.0 × 10^9 cfu/mL) were selected as representative microorganisms and cultured in a medium in an incubator. To examine the inhibitory effect of *M.bontioides* on bacteria, PAN/*M.bontioides* (3%, 5%, 7%) nanofibrous membranes were cut into 1 cm^2 squares, then incubated in 10 mL bacterial solution diluted 5 times for 24 h (dark, 37 °C). 50 μL of the solution was finally taken in solid medium and the number of colonies was observed after 12 h.

The PAN/*M.bontioides*/Ag-CN/Ag nanofibrous membranes were similarly cut into 1 cm^2 pieces and placed in a 12-well culture plate. A drop (20 μL, 1.47 × 10^9 cfu/mL) of the bacterial liquid solution was applied directly onto the nanofibrous membrane, respectively. Then, they were incubated in a dark environment for 3 h and irradiated with a xenon lamp (PLS-SXE300D, Beijing Bofillay Technology Co., Ltd.) at a light intensity of 75,000 lx for 3 h at a room temperature of 20 °C, respectively. After that, 2 mL of normal saline was added to rinse the bacteria. One drop (50 μL) of the eluate was applied uniformly to the plate of solid medium and then placed in a 37 °C incubator overnight (12 h, dark).

For the cyclic sterilization test, 20 μL of bacterial solution was applied directly to the nanofiber membrane and irradiated for 3 h. After illumination, another 20 μL of bacterial solution was painted on the above membrane and irradiated for another 3 h for cycle 2. For cycle 3, another 20 μL of bacterial solution was coated on the above-mentioned membrane for 3 h of light irradiation. After that, 2 mL of normal saline was injected to flush the bacteria. One drop (50 μL) of the eluate was spread evenly onto the solid culture plate and then kept in an incubator at 37 °C overnight (12 hr, dark).

The bacterial inhibition rate was calculated according to Eq. (7) [2,47].

$$\text{Bacteria inhibition rate} = \left(1 - \frac{\text{Number of bacteria in the experimental group}}{\text{Number of bacteria in the control group}}\right) \times 100\% \quad (7)$$

2.9. Antiviral activity assays

The sterilized PAN/*M.bontioides*/Ag-CN/Ag nanofibrous membrane (25 mm diameter circular membrane) was put on the bottom of a 12-well culture plate to which 1 mL of H3N2 had been inserted. The interaction time between the membranes and the virus solution at 4 °C was 2 h, then 100 μL of H3N2 solution was extracted, with three parallel samples taken. The amount of infectious H3N2 particles was determined based on a 50% tissue culture infectious dose (TCID50) in MDCK cells. Dilute 100 μL of H3N2 solution with Dulbecco's Modified Eagle Medium (DMEM) containing 1% trypsin and 0% serum. MDCK cells inoculated into 96-cell plates were grown to 100% and infected using a 10-fold serial dilution of H3N2. After incubation at 37 °C for 2 h, cells were washed three times with PBS and incubated for 72 h. Cytopathic effects (CPE) were monitored and counted by viewing the cell plates under an electron microscope, which was common in inoculated MDCK cells. Titers were reported as TCID50 calculated by Reed and Muench method.

Table 1
Information about the target.

Protein name	PDB ID	References
Mpro	6LU7	[64]
RdRp	6XQB	[27]
ACE2	2AJF	[16]

2.10. Molecular docking

Molecular docking of viral protein targets and potential target compounds was performed by the drug design software Discovery Studio 2017 to analyze the interactions between compounds and proteins. The relevant crystals of Mpro, RdRp and ACE2 were screened from the Research Collaboration for Structural Bioinformatics Protein Data Bank (RCSB PDB) in Table 1, imported the structures of the compounds into Discovery Studio 2017 and used the minimize module for drug structure optimization. The target protein was dehydrated and hydrogenated to convert the two-dimensional structure of the compound into a three-dimensional structure. The optimized small molecule structures were imported into the receptor- ligand interaction module for CDOCKER algorithm molecular docking. The parameters related to molecular docking were set as follows: Pose Cluster Radius was set to 0.5. Random Conformations was set to 10. Orientations to refine was set to 10. The rest of the settings were default. The binding ability of the compounds to the target protein was expressed by the -CDOCKER Energy value.

3. Results and discussion

3.1. Surface morphology of the nanofibrous membranes

In this study, the PAN/*M.bontioides*/Ag-CN/Ag nanofibrous membrane were obtained by electrospinning, in which AgNPs, Ag-CN nanopowders and *M.bontioides* plant extracts were incorporated. The surface morphological features of the samples were observed by scanning electron microscopy as described in Fig. 2. Nanofibers without any

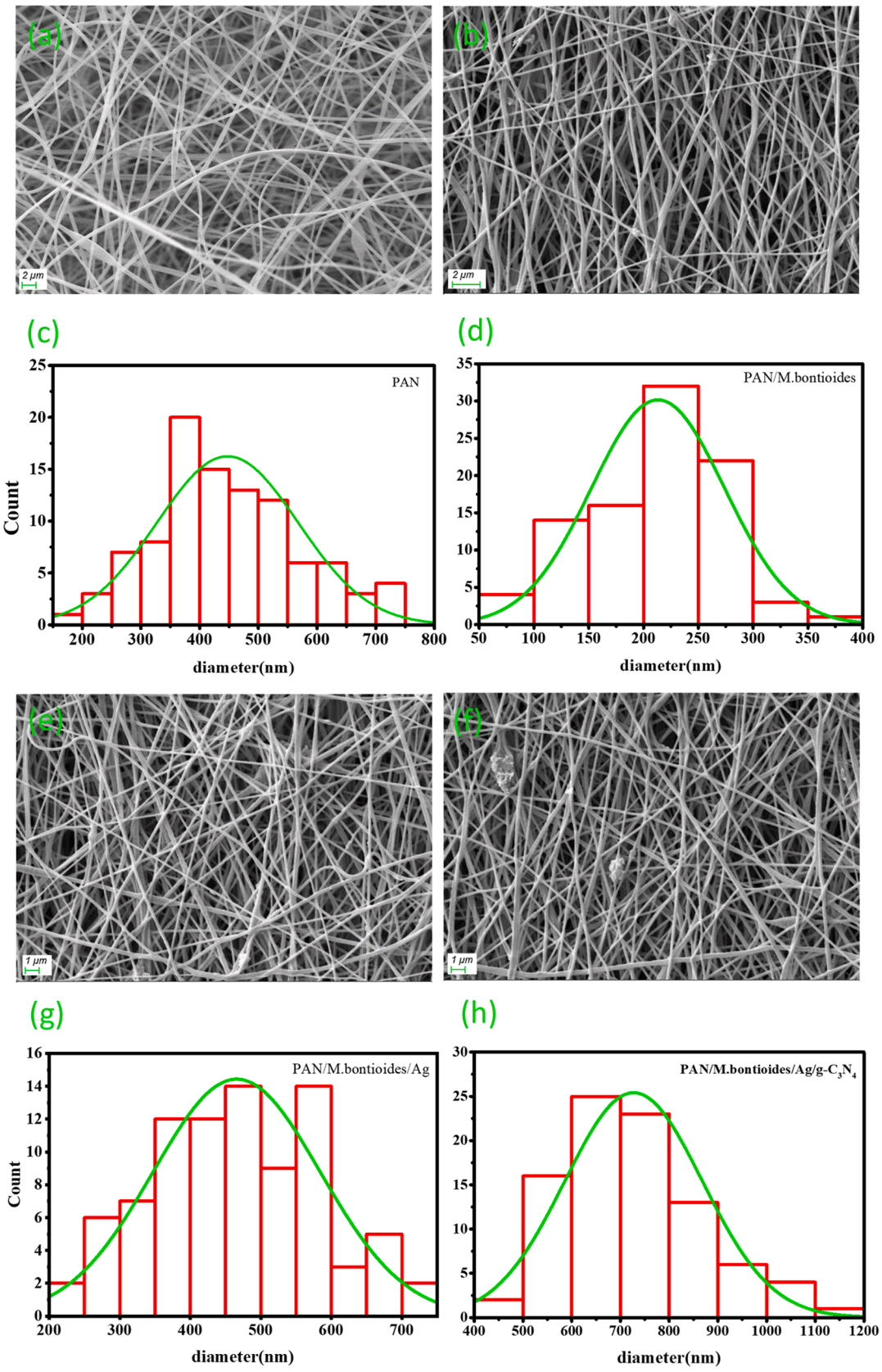

Fig. 2. SEM images and diameter analysis of PAN nanofibrous membrane (a, c), PAN/*M.bontioides* nanofibrous membrane (b, d), PAN/*M.bontioides*/Ag nanofibrous membrane (e, g), PAN/*M.bontioides*/Ag-CN/Ag nanofibrous membrane (f, h).

beads were noticed in all samples. The mean and average diameters and standard deviations of PAN, PAN/*M.bontioides*, PAN/*M.bontioides*/Ag and PAN/*M.bontioides*/Ag-CN/Ag Nanofibers were 447.48 ± 119.71 nm, 213.18 ± 60.52 nm, 465.74 ± 118.19 nm, and 726.93 ± 140.50 nm, respectively. As a special southern natural plant, the extract of *M. bontioides* contains a certain amount of solvent, mainly water or anhydrous ethanol [37,39]. When *M.bontioides* was included in the precursor solution, it reduced the viscosity of the solution, resulted in a smaller diameter of PAN/*M.bontioides* Nanofibers containing *M.bontioides*. The Ag ions were reduced to AgNPs in the presence of DMF, which will be dispersed around in the solution. Under the impact of the high conductivity of metallic silver, the ions of the precursor solution became exceptionally active when loaded with high-voltage current, and the attraction between the ions was enhanced, so that the diameter of the obtained nanofibers became larger than that of the pure PAN nanofibers [43,44,65,66]. In contrast to PAN nanofibers, PAN/M.bontioides/Ag-CN/Ag nanofibers had a rougher surface and a more heterogeneous structure, and aggregates of Ag-CN and AgNPs were observed on the surface. This increase in roughness indicated that the Ag-CN NPs were not only inside the PAN Nanofibers but also on the surface of the fibers. A difference in the diameters of the NPs was observed. Especially, the NPs containing Ag-CN were explained as a result of the enhanced viscosity and conductivity of the polymer solution and favorably reduced the ionic mobility and whipping instability during electrospinning (Table 2) [43]. It also caused an increase in the surface roughness of the nanofibers and the formation of various irregular structural features, which improved the interception of tiny particles.

3.2. SEM-mapping and TEM analysis of the nanofibrous membranes

The distribution of C, N, O, Ag and Mg elements in the PAN/*M. bontioides*/Ag-CN/Ag nanofibrous membrane was observed by SEM-Mapping to investigate the distribution of the additive inside and outside the nanofibrous membrane. As Fig. 3, all elements were uniformly distributed in the nanofibrous membrane. The carbon element was mainly derived from PAN and g-C_3N_4. While the nitrogen was originated dominantly in g-C_3N_4, there were several distinct bright spots (Fig. 3c), exhibiting agglomeration of larger clusters. It was primarily owed to the mutual attraction of electrons. Fig. 3(d-e) illustrated that *M. bontioides* contains a large number of trace metals (e.g. Mg) and active oxides. Mg was mainly derived from chlorophyll in plants, while Ag was yielded by the addition of $AgNO_3$. This indicated that the process of electrospinning was successfully applied to make the substances (e.g. *M. bontioides* extract, AgNPs and Ag-CN) uniformly dispersed on the electrospun nanofibrous membranes, thus effectively enhancing the ability and effectiveness of inhibiting and killing pathogens, and contributing to the enhancement of the protective material for the human body.

The Ag-CN powders and nanofibers were observed by transmission scanning electron microscopy (TEM, FEI/Talos L120C). Fig. 4 was the TEM image of Ag-CN powders and PAN/*M.bontioides*/Ag-CN/Ag nanofibers at different positions. As Fig. 4a, a significant amount of AgNPs were found to be bound to the g-C_3N_4 surface, which was mainly derived by photodeposition. Simultaneously, it was observed in Fig. 4b that both the surface and the interior of the nanofibers were encapsulated by many particles of different sizes. The large particles may be Ag-CN particles or clusters formed by Ag-CN and AgNPs, while the small particles may be AgNPs. The rough surface formed by such raised, folded or wrinkled areas caused by nanoparticles prevents aerosol particles on the fiber surface from sliding and stagnating, so as to obtain excellent filtration performance [46,67]. It also enhanced the contact area with pathogens to multiply the killing effectiveness. Furthermore, it was susceptible to receive more energy from sunlight and stimulate electron production of ROS [53,63].

3.3. Structural properties of the nanofibrous membranes

The fabricated different electrospun fiberous membrane composites were analyzed by XRD and FT-IR as presented in Fig. 5. To reveal the crystalline and phase structures of the prepared nanocomposites, XRD patterns were measured as demonstrated in Fig. 5a. No specific peaks were observed for the pure PAN nanofibrous membrane. The characteristic metallic silver peaks at $2\theta = 38.1^\circ$, 46.2°, 64.5° and 77.3° corresponding to (111), (200), (220) and (311) crystal planes, respectively, were observed in all samples containing cubic Ag crystal structure (JDPDF 41-0607). The characteristic g-C_3N_4 peak at 27.9°, corresponding to the (002) plane, was in existence for all the photocatalysts. The peak was attributed to the strong structural interlayer stacking of the conjugated aromatic system along the c-axis within the lattice plane. The small angular peak at 17.3° corresponding to (100) was presumably ascribed to the occurrence of a small tilt angle with the interlayer stacking structure. The mean crystal size (D) of Ag NPs and Ag-CN was estimated by Debye-Scherrer Eq. (8).

$$D = \frac{0.9\lambda}{\beta \bullet cos\theta} \tag{8}$$

where λ, θ and β were the wavelength, peak Bragg angle and the half-height width of the peak, respectively. The mean crystal size of Ag-CN was calculated to be 20.1 nm, while the average crystal size of Ag NPs was 19.1 nm. No other characteristic peaks were found in the XRD patterns apart from g-C_3N_4 and Ag, which affirmed the high purity of the PAN/*M.bontioides*/Ag-CN/Ag nanofibrous membrane.

In the FT-IR spectrum (Fig. 5b), a broad absorption peak of 3433 cm^{-1} can be observed, which was the stretching vibration of the N-H and O-H groups of the physically adsorbed water molecules. The peak at 1200–1650 cm^{-1} corresponded to the typical stretching pattern of the C-N heterocycle. the signal at 822 cm^{-1} was the characteristic absorption peak of the triazine unit. The bands around 1000 and 1150 cm^{-1} were the specific absorption vibration peaks of PAN. With the addition of Ag-CN and *M.bontioides*, the intensity of the individual absorption peaks had changed significantly. This illustrated that the nanofiber materials of complex systems prepared by electrospinning method can still maintain the stability of the structure and components of various additives without reducing the reduction of their effective functions.

3.4. Photocatalysis performance and mechanism of the nanofibrous membranes

The photocatalytic activity of the pure PAN, PAN/*M.bontioides*, PAN/*M.bontioides*/Ag, and PAN/*M.bontioides*/Ag-CN/Ag nanofibrous membranes was evaluated by the photodegradation of the MB solutions, as described in Fig. 6. The degradation efficiency of MB was determined by investigating the difference in the absorption value of MB at 663 nm. In Fig. 6a, the decrease in absorbance of the MB solution was exhibited for the period 0–150 min. The degradation efficiency of pure PAN for MB

Table 2
Viscosity and Conductivity of the electrospinning precursor fluid.

Samples	PAN	*M. bontioides*	Ag	Ag-CN	Viscosity/(mPa s)	Conductivity/(ms cm^{-1})
PAN	8 wt%	/	/	/	1650 ± 0.82	0.0891 ± 0.0037
PAN/*M. bontioides*	8 wt%	5 wt%	/	/	266 ± 1.63	0.1023 ± 0.0005
PAN/*M. bontioides* /Ag	8 wt%	5 wt%	5 wt%	/	340.33 ± 2.87	1.7537 ± 0.0021
PAN/*M. bontioides*/Ag-CN/Ag	8 wt%	5 wt%	5 wt%	1 wt%	405.67 ± 2.87	2.4267 ± 0.0170

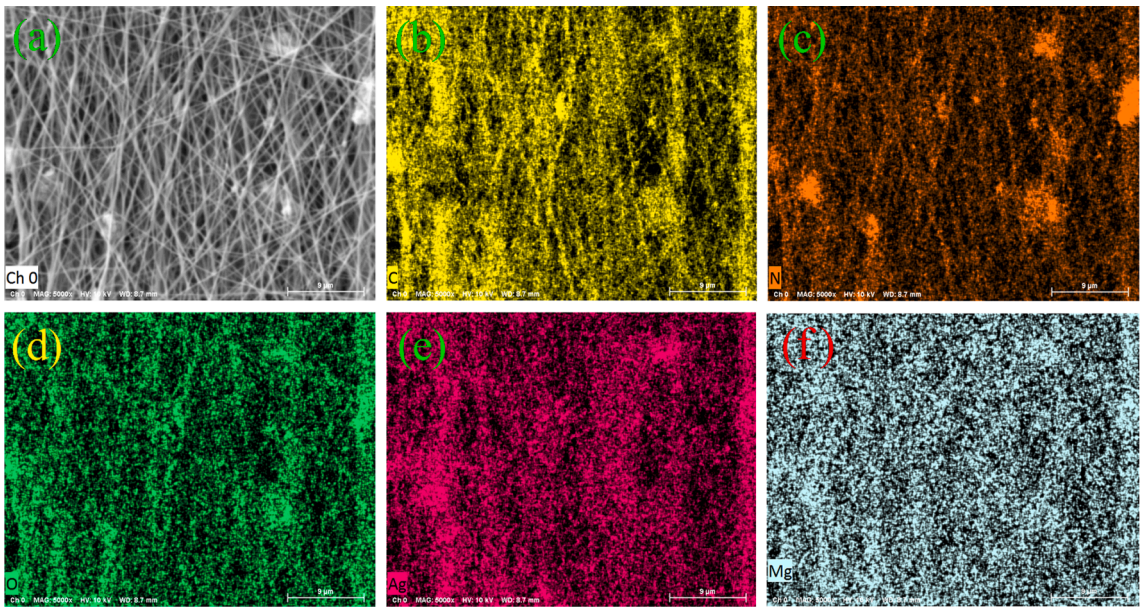

Fig. 3. SEM-mapping of the PAN/*M.bontioides*/Ag-CN/Ag nanofibrous membrane. (a) SEM images of PAN/*M.bontioides*/Ag-CN/Ag nanofibrous membrane. (b) C, (c) N, (d) O, (e) Ag, (f) Mg.

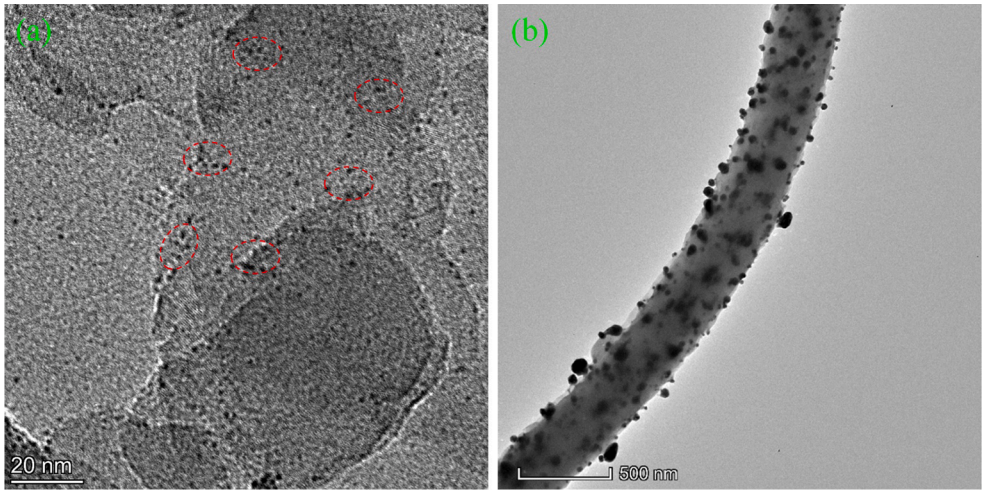

Fig. 4. TEM images of Ag-CN (a) and PAN/*M.bontioides*/Ag-CN/Ag nanofibers (b).

was only 3.86% (Fig. 6c), with no significant photocatalytic activity. This was attributed to the fact that pure PAN nanofiber membranes prepared by the electrospinning process carried electrostatic charges and attracted free MB molecules in the MB solution [61,68]. When *M. bontioides* and Ag were included, 81.05% and 89.29% (Fig. 6c) of the MB degradation efficiency was achieved, respectively. PAN nanofibrous membrane with *M.bontioides* and Ag-CN had revealed the highest MB photodegradation efficiency of 96.37% (Fig. 6c).

The slope of $\ln(C_0/C_t)$ plotted as a linear function of time for the fabricated mats (Fig. 6b) corresponded to the pseudo-first-order rate constant k (min^{-1}) (Fig. 6d), and the half-life was calculated by Eq. (3) to (5). The value of slope k for pure PAN was close to 0 and negligible. The calculated half-life and rate constants of the PAN/*M.bontioides*, PAN/*M.bontioides*/Ag, PAN/*M.bontioides*/Ag-CN/Ag nanofibrous membrane were 64.18 min and 0.0108 min^{-1}, 47.15 min and 0.0147 min^{-1}, 32.24 min and 0.0215 min^{-1}, respectively. When xenon light was shone on the nanofiber membrane and the MB solution, the MB molecules became more active and easily bound to the trace metals (Ag, Fe) and Ag from *M. bontioides* extract in the nanofiber membrane, while the nanofiber membrane also carried the electrostatic charge, causing the MB molecules to cling to the nanofiber membrane and a decrease in the absorbance of the solution. The MB degradation rate was accelerated up to 1.46–1.99 times after the addition of the photocatalyst g-C_3N_4. This meant that the PAN/*M.bontioides*/Ag-CN/Ag nanofibrous membrane had an effective photocatalytic degradation capability. In addition, the transient photocurrent response captured the change of photocurrent before and after binding Ag.

The photocurrent of g-C_3N_4 after binding Ag increased by several times compared to that of pure g-C_3N_4 (Fig. 6e), and the electrochemical impedance of g-C_3N_4 after binding Ag was lower than that of pure g-C_3N_4 (Fig. 6f), which indicated that Ag-CN had a low energy barrier and could more easily convert the solar energy, into other energy, such as

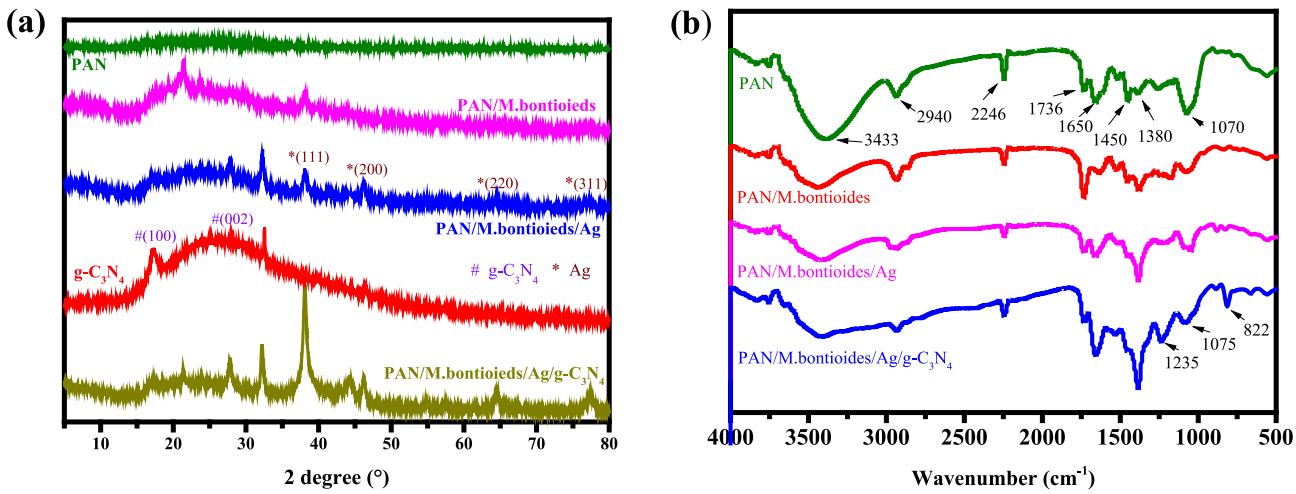

Fig. 5. XRD and FT-IR of the nanofibrous membranes. (a) XRD patterns of pure PAN, PAN/*M.bontioides*, PNA/*M.bontioides*/Ag and PAN/*M.bontioides*/Ag-CN/Ag, (b) FT-IR spectra of pristine PAN, PAN/*M.bontioides*, PNA/*M.bontioides*/Ag and PAN/*M.bontioides*/Ag-CN/Ag.

chemical energy. It was also confirmed that Ag-CN can be used as a photocatalytic antibacterial agent. In conclusion, the PAN/*M.bontioides*/Ag-CN/Ag nanofibrous membranes were proven the ability of photocatalytic degradation and could rapidly clean the surface of the fiber by removing the contaminants.

Various reactive oxygen species were observed to have an inhibitory inactivating effect on pathogens such as bacteria and viruses, and the addition of photocatalyst Ag-CN to the nanofiber membrane facilitates the production of reactive oxygen species ROS. When the PAN/*M.bontioides*/Ag-CN/Ag nanofibrous membrane was irradiated by sunlight, the photon energy was higher than the bandgap of g-C_3N_4 (2.7 eV), where the electrons (e^-) were transferred from the valence band (VB) to the conduction band (CB) while leaving the same number of photogenerated holes (h^+) in the VB. The optically excited electrons can be transferred from g-C_3N_4 to the CB of Ag, which was narrower than the CB of g-C_3N_4. Electrons accumulated at the CB of Ag or g-C_3N_4 can be transferred to oxygen molecules adsorbed on the surface to form radicals such as $\cdot O^{2-}$, HOO· and ·OH, while photoexcited holes reacted with surface-bound water molecules to produce ·OH radicals (Fig. 7). The various reactions were explained with Eq. (9) to (14) [54,58-60]. A large amount of the reactive oxidation species being produced will react with the surrounding dyes and other contacts, or enter the interior of the pathogen, destroying protein function and DNA, as well as disrupting bacterial cell membranes, which will cause the death of the pathogen and result in antibacterial and antiviral effects [61,68].

$$g - C_3N_4 + h\nu \rightarrow g - C_3N_4(h + e) \quad (9)$$

$$g - C_3N_4(e) + Ag \rightarrow g - C_3N_4 + Ag(e) \quad (10)$$

$$Ag(e) + O_2 \rightarrow O_2^- + Ag \quad (11)$$

$$O_2^- + e^- + 2H^+ \rightarrow H_2O_2 \quad (12)$$

$$H_2O_2 + e^- \rightarrow {}^{\cdot}OH + OH^- \quad (13)$$

$$OH^- + h^+ \rightarrow {}^{\cdot}OH \quad (14)$$

The electron paramagnetic resonance (EPR) spectra of xenon lamp irradiation for 10 min were recorded to investigate the production of ROS. The intense signals of DMPO-•OH and DMPO-$\bullet O^{2-}$ were successfully captured in the solution after 10 min of xenon lamp light as depicted in Fig. S2. However, no signal was detected in the EPR spectrum under dark conditions. the EPR results confirmed that the radicals produced by PAN/*M.bontioides*/Ag-CN/Ag nanofibrous membrane were mainly •OH and $\bullet O^{2-}$, which also supported the conclusion of the photocatalytic mechanism.

3.5. Particulate filtration effficiency

The filterability and breathability were measured by filtering NaCl aerosols that simulate viral and bacterial filtration. To effectively evaluate the filterability of the nanofibrous membranes, we used sodium chloride aerosol with diameters of about 70–80 nm, even smaller than SARS-CoV-2 virus with diameters of about 100 nm [18,63]. The efficiency of the filter was tested with an automatic filter tester (Model 8130, TSI, Shoreview, Minnesota, MN.USA). It was observed as Table 3 that the gas flow rate was 85 L/min, the concentration of NaCl aerosol was 20 mg/m^3, while the experimental temperature was kept at 21.3 °C and the relative humidity was 36%. The filtration efficiency of the nanofibrous membranes reached 99.82 ± 0.016% in the loading experiment, while that of the unloaded experiment reached 99.97 ± 0.013%. That indicated that the nanofibrous membranes satisfied the basic requirement of high filtration efficiency for masks. The pressure drop was the differential pressure value generated by the filtration process. The smaller the value, the better the comfort level [17,46]. With the addition of *M.bontioides* and Ag-CN, the filtration efficiency of the the nanofibrous membranes was improved and the pressure drop was reduced from 133 Pa to 64 Pa shown in Table 4. The overall filtration performance of an air filter considering efficiency and pressure drop was evaluated by the quality factor (QF). A higher QF value normally meant better overall filtration performance. The calculated QF values of the membranes based on Eq.14 were listed in Table 4. The QF value of PAN/*M.bontioides*/Ag-CN/Ag (0.097 Pa^{-1}) was significantly more than that of PAN (0.029 Pa^{-1}). It meant that the PAN/*M.bontioides*/Ag-CN/Ag nanofibrous membranes had promising overall filtration performance and was expected to be an alternative for mask filtration.

As shown in Fig. 8a, the nanofibrous membranes were laid on an automatic filtration tester to determine the upstream aerosol above the membranes and the downstream aerosol after the mat was filtered to calculate the filtration efficiency. Concurrently, the airflow and pressure through the mat were detected by sensors to represent the breathability of the mat. The filtering mechanism of the nanofibrous membranes was described in Fig. 8b, where the large particles were physically captured by inertial impact and interception of the fiber network [21], while small particles were hindered by diffusion. The microstructure of the obtained electrospun nanofibrous membranes was composed of numerous nanofibers with greater microporous porosity and larger

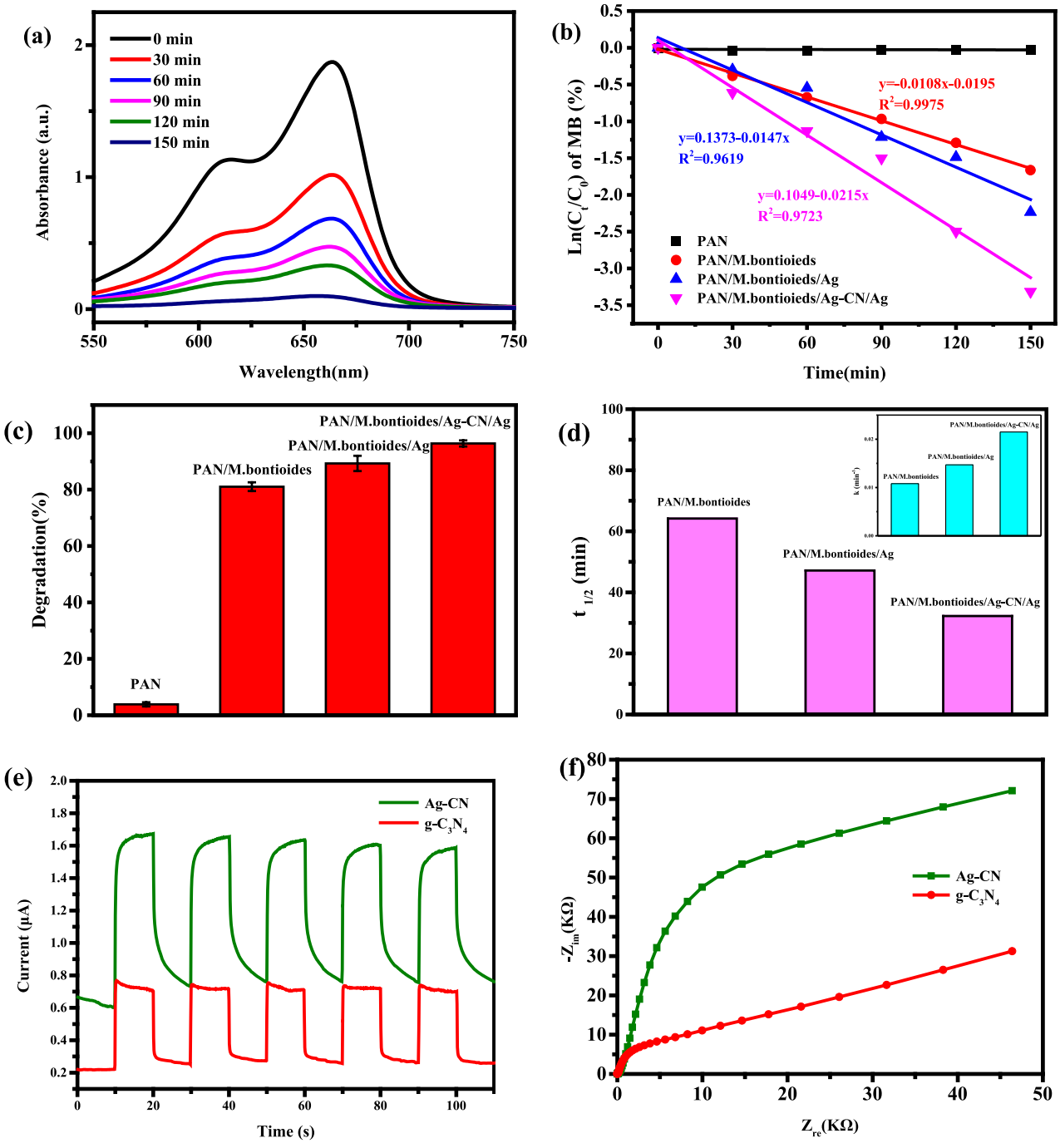

Fig. 6. Photocatalytic activity of the nanofibrous membranes. (a) UV–Vis absorbance of MB aqueous solutions transferred on the PAN/*M.bontioides*/Ag-CN/Ag nanofibrous membrane at time intervals from 0 to 150 min. (b) Plot of photocatalytic activity of the nanofibrous membrane as a function of time. (c) Photocatalytic degradation (%) of MB on the pure PAN, PAN/*M.bontioides*, PNA/*M.bontioides*/Ag and PAN/*M.bontioides*/Ag-CN/Ag nanofibrous membrane. (d) Half-life time of the photocatalytic degradation rate. The inset presents the pseudo-first-order reaction rate constant. (e) Photocurrent responses of Ag-CN and g-C_3N_4, (f) electrochemical impedance spectra of Ag-CN and g-C_3N_4.

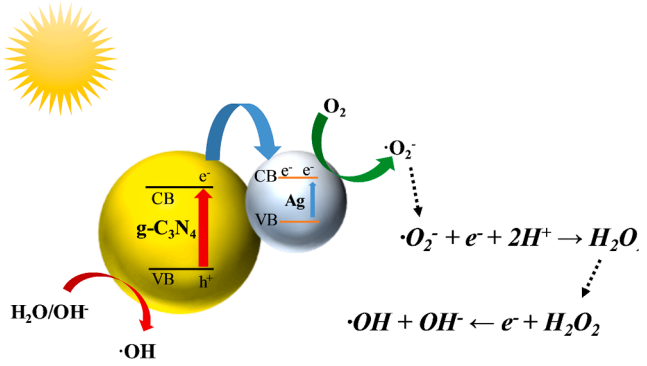

Fig. 7. Proposed mechanism of generation of ROS by Ag-CN.

Table 3
NaCl particle filtration test results of the nanofibrous membranes.

Test items	Test Conditions	Test results		Average ± Standard deviation
NaCl particulate matter filtration efficiency (η)/ [%]	Gas flow rate: 85 L/min Aerosol particles: NaCl Aerosol Concentration: 20 mg/m^3 Temperature: 21.3℃ Relative humidity: 36%	1#	99.801%	99.82 ± 0.019%
		2#	99.839%	
		3#	99.822%	
		4#	99.989%	99.97 ± 0.013%
		5#	99.958%	
		6#	99.968%	
Pressure drop (ΔP)/ [Pa]	Gas flow: 85 L/min	1#	58 Pa	59 ± 5.57 Pa
		2#	65 Pa	
		3#	54 Pa	
		4#	74 Pa	70.67 ± 4.16 Pa
		5#	66 Pa	
		6#	72 Pa	

Samples 4#, 5#, and 6# were not subjected to loading test.

contact area to filter tiny particles. Besides physical filtration, there was an electrostatic attraction to the particles. During the experiment, positive/negative electrodes were connected to each of the solution and the receiver, and a voltage of 17 kV was applied. Then, under the action of electric field force, nanofibers carrying a large amount of positive/negative charges flew toward the collector, and nanofiber films were formed during the rotation. After the experiment, the electrostatic charges loaded on the nanofiber membrane will not disappear immediately, so the nanofiber membrane will still carried a large amount of electrostatic charges and had an electrostatic attraction effect on the particles.

To further simulate the application of nanofiber membranes in practice, the PAN and PAN/*M.bontioides*/Ag-CN/Ag nanofiber membranes were placed in an environment with 85% humidity for 30 min, and then an airflow of 85 L/min was applied for 30 s. After the experiment, the surface morphology was observed by SEM (ZEISS EVO MA 15). The nanofibers were subjected to the impact of airflow and the surface morphology changed, and some of the nanofibers adhered to each other as depicted in Fig. S3, but the overall nanofiber membrane filtration performance was not greatly affected. Thus, the obtained nanofibrous membranes by an electrospinning process exhibited excellent filtering properties.

3.6. Antimicrobial activity

M.bontioides containd a variety of terpenoids and flavonoids that were proved to have inhibitory effects on various bacteriasm [37-39]. It was evaluated by *E. coli* (Gram-negative bacteria) and *S. aureus* (Gram-positive bacteria) to determine the antibacterial and antimicrobial effects of *M.bontioides*. Pure PAN and *M.bonioides* with 3 wt%, 5 wt%, and 7 wt% PAN/*M.bonioides* nanofibrous membranes were studied (Fig. 9). With the accumulation of the amount of *M.bontioides*, the antibacterial effect became increasingly apparent. When the amount of *M.bontioides* was 3 wt%, the inhibitory effect on *E. coli* was 64.68%, while the inhibitory effect on *S. aureus* was 69.23%. At the content of 5 wt%, the inhibitory effects on *E. coli* and *S. aureus* were 97.37% and 95.99%, respectively. Once the content reaches 7 wt%, it showed a strong inhibitory effect on both *E. coli* and *S. aureus*, up to 99.50% and 98.08%, respectively. The inhibitory activity of *M.bontioides* was principally connected with the number of hydroxyl groups on the aromatic ring of flavonoids and the position of hydroxyl groups [69-71]. The specific mechanism may be (Fig. 10): (1) by controlling the tricarboxylic acid cycle pathway in the sugar metabolism pathway of the test strain; (2) by impeding the uptake of energy substances and inhibiting their growth and recovery; (3) by suppressing the activity of reductase to inhibit the synthesis of the cell membrane, as well as by generating hydrogen peroxide to damage the cytoplasmic membrane to achieve the inhibition; (4) by causing protein coagulation or denaturation.

To evaluate the antimicrobial properties of the prepared nanofibrous membrane, PAN/ *M.bontioides*/Ag-CN/Ag was evaluated against *E. coli* and *S. aureus*. The filter layer of the commercial mask was selected as the control group. 20 μL of bacterial solutions were dropped on nanofiber membranes and incubated in the dark and under a xenon lamp with a light intensity of 7500 lx for 3 h, respectively. In the dark environment, the PAN/*M.bontioides*/Ag-CN/Ag nanofibrous membrane had an inhibitory effect on *E. coli*, as in Fig. 11a, as well as of *S. aureus*, in Fig. 11b. It was the AgNPs and *M.bontioides* in the nanofiber membrane played an important role to inhibit the growth amount of bacteria. The inhibition results of *E. coli* were better than that of *S. aureus*, the reason was that the growth conditions of *E. coli* required low and fast proliferation, and the maximum bacterial capacity was easily reached after 12 h of incubation, and when AgNPs and *M.bontioides* were released, a large number of bacteria could be killed quickly. While *S. aureus* proliferates slowly, 12 h of incubation did not reach the maximum bacterial capacity, and when AgNPs and *M.bontioides* were delivered, there were still some bacteria kept dividing and proliferating. No live *E. coli* (Fig. 11a) and *S. aureus* (Fig. 11b) were detected in all samples after 3 h of irradiation using a xenon lamp, which indicated that the prepared nanofibrous membranes were more effective in killing bacteria under light conditions. The experimental results under light conditions were better compared to those under dark conditions, because the photocatalyst Ag-CN added played a crucial role in the photocatalytic reaction, producing a lot of active ROS that caused the death of massive bacteria.

Table 4
The filtration performances of the nanofibrous membranes.

Samples	Filtration effificiency (%)	Pressure drop (Pa)	Quality factor (Pa^{-1})	Face velocity	Reference
PAN	96.12	133	0.024	0.21 m/s	Yanyun Ju et al. [46]
PAN	97.38	126	0.029	0.2 m/s	This work
PAN/*M.bontioides*/Ag-CN/Ag	99.82	65	0.097	0.29 m/s	This work

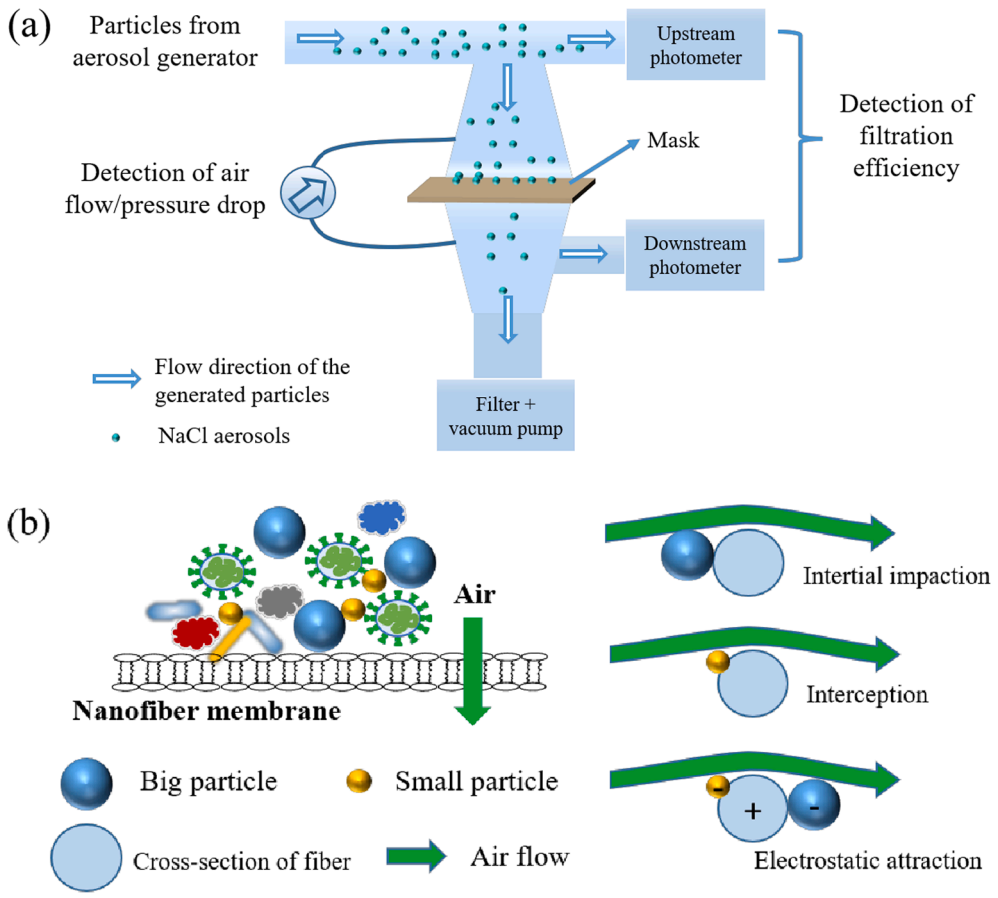

Fig. 8. Airflow, and particle filtration of the nanofibrous membranes. (a) Schematic diagram of a mask measuring filtration efficiency, (b) The mechanism of filtering particulate matter by a mask.

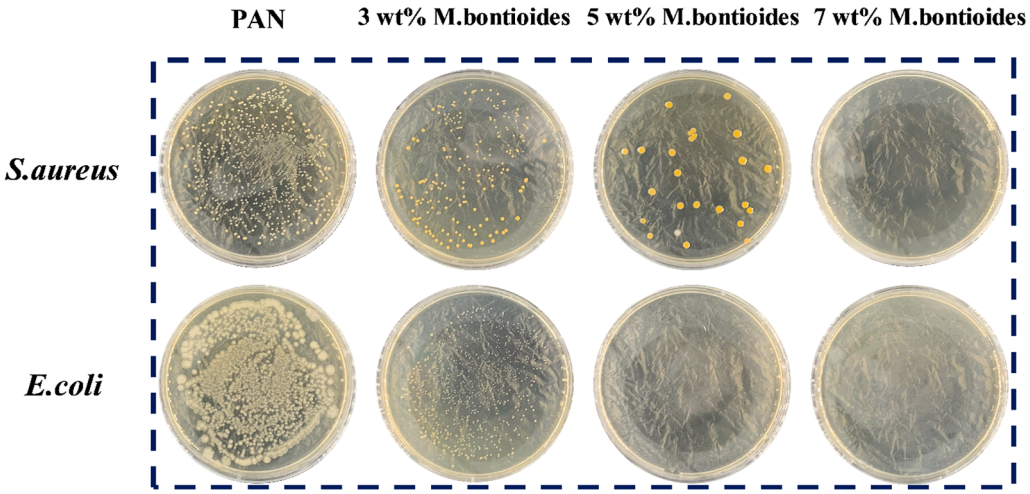

Fig. 9. The antibacterial test of the PAN/*M.bonioides* nanofibrous membranes with different *M.bontioides* concentrations.

The antibacterial effect of the samples was verified by monitoring the viability of *E. coli* (Fig. 11c) and *S. aureus* (Fig. 11d) at different light times. The reason why we chose 3 h of illumination was to ensure that the illumination time was long enough to kill all bacteria before the next cycle test. It can be evident that the number of *E. coli* growing on the samples gradually decreases with passing time, such as Fig. 11c. The average inhibition rates for 1 h, 2 h and 3 h were calculated as 76.97 ± 0.71%, 88.58 ± 2.80% and 98.65 ± 1.49% after three cycles, correspondingly. In addition, the PAN/*M.bontioides*/Ag-CN/Ag nanofibrous membrane had demonstrated excellent antibacterial activity against *S. aureus* (Fig. 11d). After 3 h of illumination, *S. aureus* was substantially eliminated. The inhibition rates for 1 h, 2 h and 3 h against *S. aureus* were 31.84 ± 2.33%, 79.26 ± 3.82%, and 97.8 ± 1.27%, respectively. Encouragingly, after three cycles, *E. coli* and *S. aureus* were virtually eliminated, which indicated that the PAN/*M.bontioides*/Ag-CN/Ag nanofibrous membranes had a remarkable cyclic bactericidal effect.

To closely match the application in practice, the nanofiber membrane was placed in an environment with 85% humidity for 30 min, and

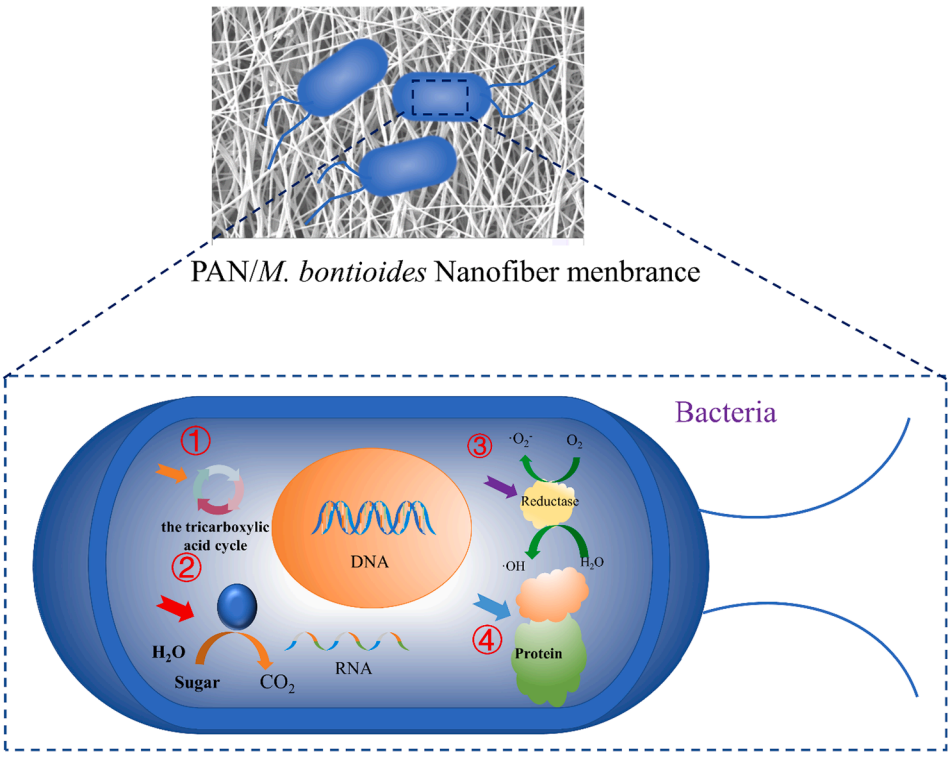

Fig. 10. Specific mechanism of the inhibitory activity of the PAN/*M.bonioides* nanofibrous membranes.

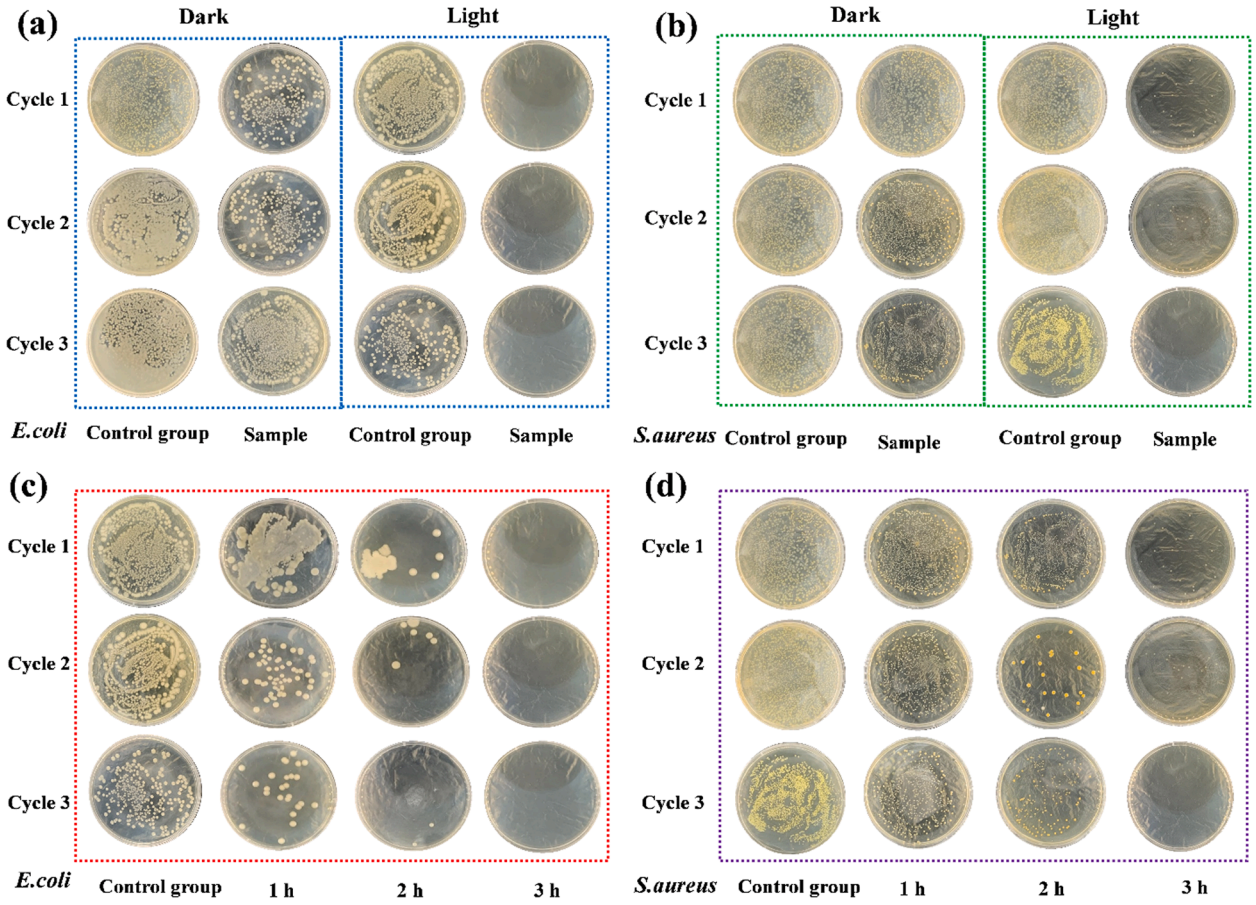

Fig. 11. Photocatalytic antibacterial test. Antibacterial results of the PAN/*M.bontioides*/Ag-CN/Ag nanofiber membranes in 3 cycles of experiments incubated under dark conditions for 3 h (a) and under xenon light irradiation for 3 h (b). Inhibition results of the PAN/*M.bontioides*/Ag-CN/Ag nanofiber membranes irradiated with xenon lamp for different times against *E. coli* (c) and *S. aureus* (d) in 3-cycle experiments. The control group are the filter layers of commercial masks.

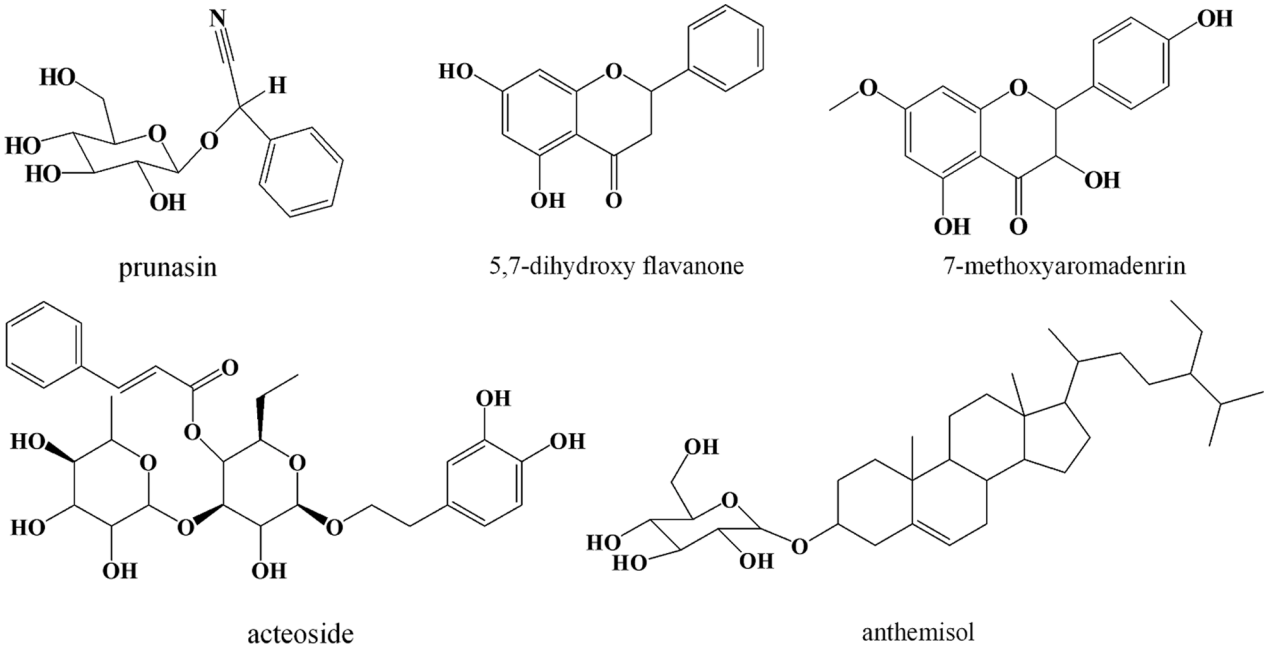

Fig. 12. Structure of selected compounds in *M.bontioides*.

Table 5
The docking situation between Mpro, RdRp and ACE2 and compounds of *M. bontioides*.

Protein Name	Target Point (PDB ID)	Docking radius	Compounds	-CDocker Internation Energy
Mpro	6LU7	13.8214	prunasin	37.774
			acteoside	71.9157
			5,7-dihydroxy flavanone	30.5644
			anthemisol	50.2534
			7-methoxyaromadenrin	40.4454
RdRp	6XQB	17.1374	prunasin	4.23179
			acteoside	25.3492
			5,7-dihydroxy flavanone	5.96044
			anthemisol	20.9511
			7-methoxyaromadenrin	8.67025
ACE2	2AJF	34.7755	prunasin	0
			acteoside	−0.00289805
			5,7-dihydroxy flavanone	0.030233
			anthemisol	0.0166443
			7-methoxyaromadenrin	0.00073645

then the antibacterial activity of the nanofiber membrane was tested under dark and light conditions. It was noticed that the nanofiber membranes still presented good antibacterial activity under dark and light conditions (as in Fig. S3). The main reason was that the environment with 85% humidity not only increased the chance of contact between substances such as AgNPs and bacteria, but also promoted the production of ROS.

The antibacterial mechanism was probably: (1) the sample was illuminated by xenon light, the Ag-CN took an electron leap, resulting in a large amount of ROS [53,63]. ROS could damage bacterial cell membranes together with AgNPs, and the destruction of cell walls or cell membranes could interfere with protein synthesis and processing, prevent DNA replication, and cause leakage of intracellular components. (2) the additives (*M.bontioides*, AgNPs and ROS) enter the interior of the pathogen, which disrupted protein function and DNA, and affected the uptake and conversion cycle of sugars, leading to the death of the pathogen.

3.7. Molecular docking

The novel coronavirus (SARS-CoV-2) is a beta coronavirus with 11 functional genes encoding structural, nonstructural, and accessory proteins [72,73]. Structural proteins include spike proteins (S), cytosolic proteins, membrane proteins, and nucleocapsid proteins [74,75]. The S proteins are the major antigens for coronavirus-induced neutralizing antibodies and are better proteins for vaccine studies [76-78]. The nonstructural proteins contain the important two proteins from SARS-CoV-2: Mpro and SARS-CoV-2 RNA-directed RNA polymerase (RdRp) [78,79]. These two proteins (Mpro, RdRp) are involved in the replication and transcription of the virus. After the virus infiltrates the cell, it enters the cell by interacting with the host cell proteins. The most clearly identified protein in the organism that interacts with neocoronavirus is angiotensin-converting enzyme 2 (ACE2). As a result, screening for small molecule active drugs had focused on Mpro, RdRp, and ACE2.

-CDocker Internation Energy is an indicator for the evaluation of the results of molecular docking under the CDOCKER algorithm [80]. The molecular docking is measured by the energy value, and it was commonly accepted that the smaller the docking radius and the higher the energy value, the better the result [81]. The compounds prunasin, acteoside, 5,7-dihydroxy flavanone, anthemisol, and 7-methoxyaromadenrin in *M.bontioides* (Fig. 12) were selected for molecular docking simulations with protein targets, where the target point of Mpro was 6LU7, the target point of RdRp was 6XQB, and the ACE2 target point was 2AJF. The docking between Mpro, RdRp and ACE2 with the compounds was shown in Table 5. It was concluded that the targets of compound action were mainly focused on two proteins, Mpro and RdRp, where the docking energy of the compound with Mpro was the highest and the docking radius was the shortest. The docking radius from longest to shortest was: 2AJF > 6XQB > 6LU7. The docking energies for targeting with 6LU7 were from highest to lowest: acteoside > anthemisol > 7-methoxyaromadenrin > prunasin > 5,7-dihydroxy flavanone. For the 6XQB target, the docking energy was in descending order: acteoside > anthemisol > 7-methoxyaromadenrin > 5,7-dihydroxy flavanone > prunasin. In descending order of docking energy with 2AJF target: 5,7-

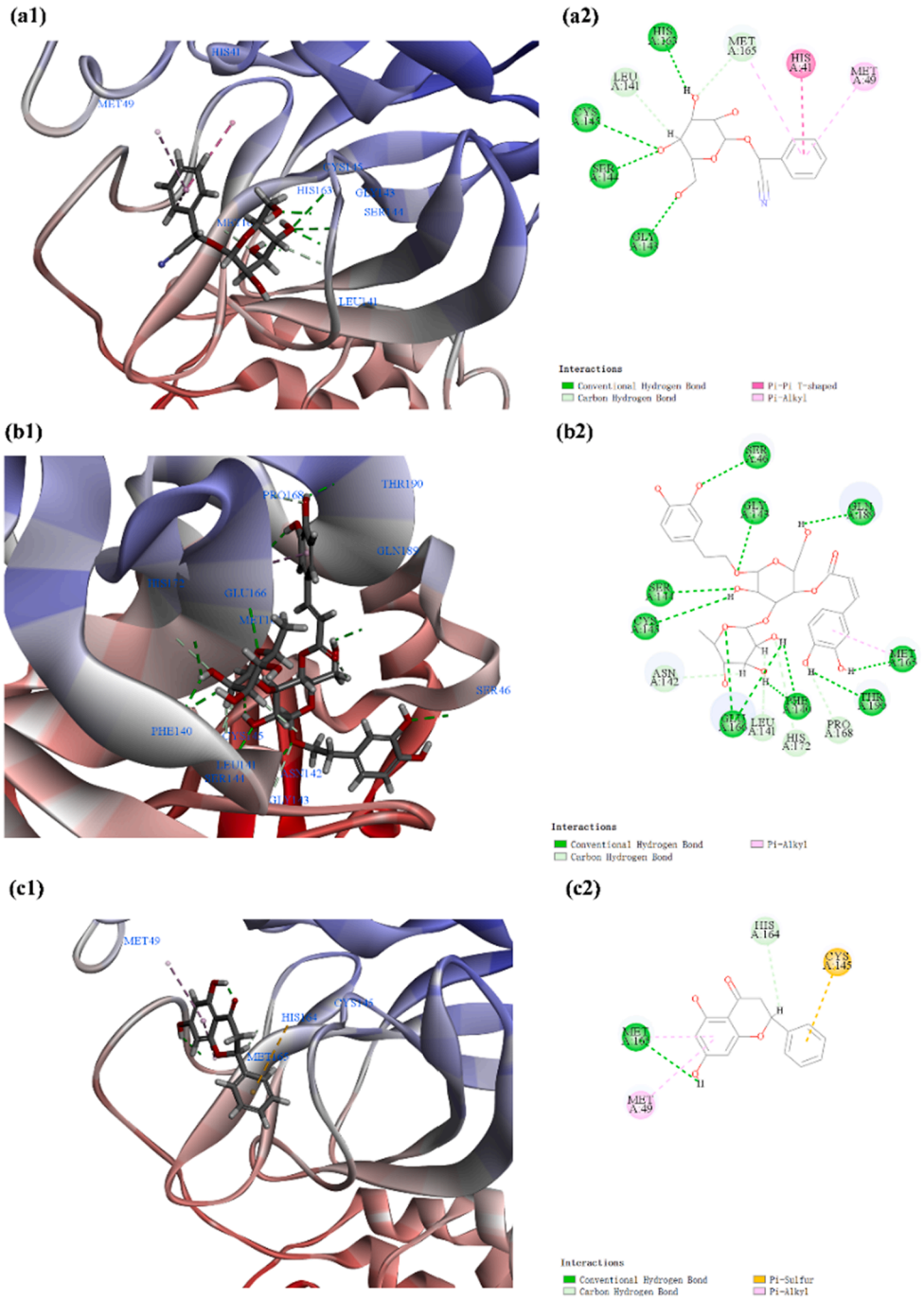

Fig. 13. The 3D and 2D molecular binding models. (a1-e1) were three-dimensional spatial binding models for small molecule compounds and protein receptors 6LU7 targets, (a2-e2) were the structures of small molecule compounds with their surrounding key amino acid binding sites. a: prunasin, b: acteoside, c: 5,7-dihydroxy flavanone, d: anthemisol, e: 7-methoxyaromadenrin.

dihydroxy flavanone > anthemisol > 7-hydroxyaromadenrin > prunasin > acteoside. The compound acteoside had the highest docking energy with the 6LU7 target and the 6XQB target, implying that acteoside was most promising to affect the process of neo-coronavirus replication and transcription.

The 3D and 2D molecular binding models were presented in Fig. 13. 3D diagrams illustrated the 3D spatial binding model of a small molecule compound and a protein receptor 6LU7 targets, while 2D diagrams showed the structure of the compound with its surrounding key amino acid binding sites. Table 6 provided the number of amino acid binding sites for *M.bontioides* compounds at the 6LU7 target site (from largest to smallest): acteoside > prunasin = 7-methoxyaromadenrin > anthemisol > 5,7-dihydroxy flavanone. The compound acteoside had the maximum bound sites to amino acids around the 6LU7 target site. The 3D and 2D plots in Fig. 13 identified that the *M.bontioides* compound combined to multiple amino acids around the 6LU7 target site, which may prevent it from participating in the replication and transcription process of the virus and reduce the quantity of the virus. The results illustrated that the *M.bontioides* extract had an inhibitory effect on SARS-CoV-2 virus, which also indicated that the incorporation of the *M.bontioides* extract into nanofiber materials to counteract the virus was feasible. *M.bontioides* is an herbal plant that can be cultivated on a large scale and widely used,

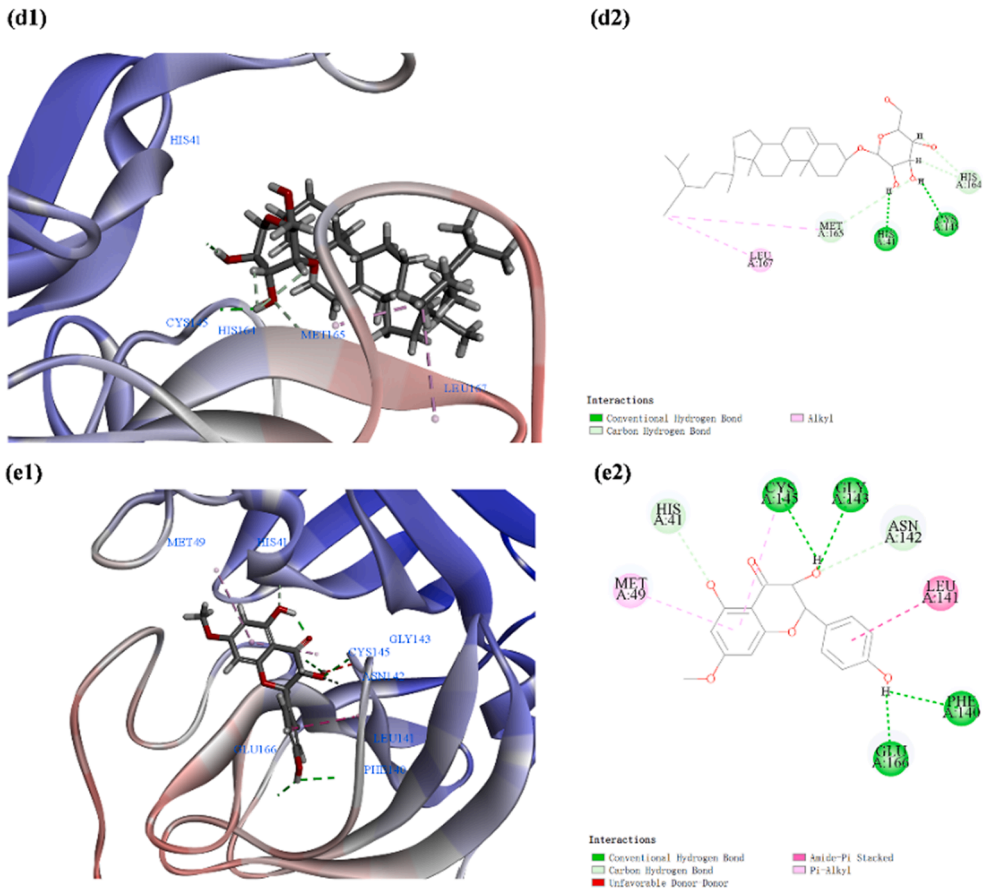

Fig. 13. (*continued*).

Table 6
Number of amino acid binding sites of the *M.bontioides* compounds at the 6LU7 target site.

Compounds	prunasin	acteoside	5,7-dihydroxy flavanone	anthemisol	7-methoxyaromadenrin
Number of amino acid binding sites to the 6LU7 target site	8	13	4	5	8

Table 7
Antiviral activity of the PAN/M.bontioides/Ag-CN/Ag nanofibrous membranes against H3N2 influenza virus.

Experimental virus	No.	Virus titer (Vb) of control samples 0 h after inoculation	Virus titer (Vc) of control samples 2 h after inoculation	Virus titer (Vc) 2 h after test sample inoculation
Influenza A virus H3N2 (ATCC VR-1679. MDCK cells as host)	1	6.2	5.57	5.46
	2	6.12	5.50	5.31
	3	6.12	5.5	5.4
Log TCID50 of the mean virus titer / mL		6.15	5.52	5.39
Log TCID50 of the mean virus titer / cm^2		5.95	5.32	2.73

with green features and great potential for future applications.

3.8. Antiviral activity

Influenza A H3N2 is a subtype of influenza A virus and is one of the major human seasonal influenza viruses. It is characterized by high frequency of influenza A mutation and rapid antigenic drift, which poses a serious threat to human health and brings great pressure to public health prevention and control. Therefore, influenza A virus H3N2 was selected as the virus source and c was cut into 25 mm diameter discs for a series of tests, and the results were listed in Table 7. The amount of H3N2 virus was determined by 50% of the tissue culture infectious dose (TCID50) in MDCK cells, and the antiviral activity of the nanofibrous membrane was assessed by the logarithmic decrease value of the control titer at the end of the indicated incubation period. Compared to the control, after 2 h exposure of the PAN/*M.bontioides*/Ag-CN/Ag nanofibrous membrane to H3N2 virus, a decrease in the log TCID50 of the mean virus titer was found after 2 h of test sample inoculation, with the log TCID50 of the mean virus titer per mL decreasing from 5.52 to 5.39; The log TCID50 of the mean virus per cm^2 titer decreased from 5.32 to 2.73. The reduction of H3N2 virus implied that the PAN/*M.bontioides*/Ag-CN/Ag nanofibrous membrane has antiviral activity against H3N2 virus.

The mechanism of this inhibition could be that the ions of *M.bontioides* extracts and AgNPs disrupt the structural integrity of the lipid bilayer membrane or the surface antigens of the viral particles, affecting

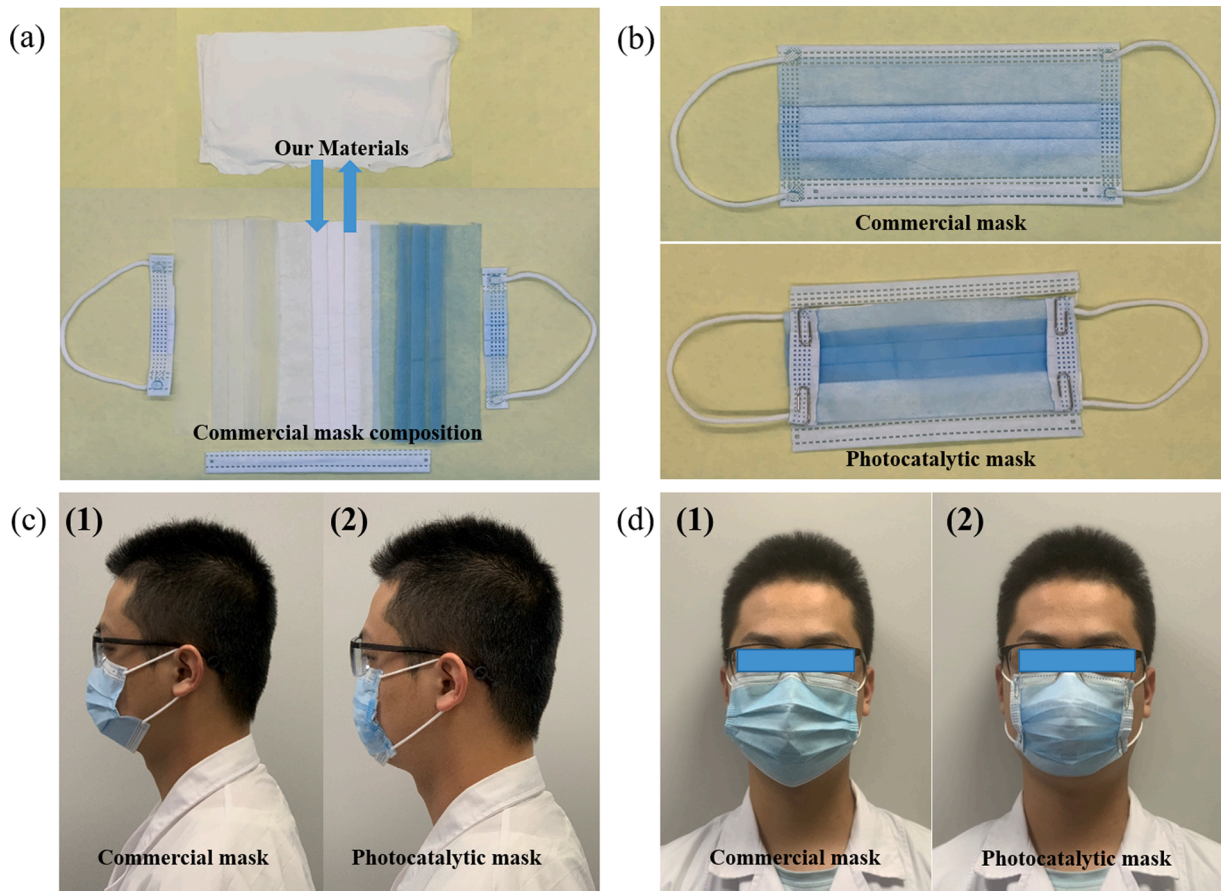

Fig. 15. Prototype of photocatalytic mask and filtration efficiency after wearing. (a) A prototype mask is manufactured by substituting the filter of a commercial mask with PAN material. (b) Photographs of a prototype photocatalytic mask and a commercial mask. (c) Side view and (d) front view of the commercial mask (1) and the photocatalytic prototype mask (2) worn by the author.

Table 8
Questionnaire results of photocatalytic prototype masks on appearance, filtration effect and comfort.

Evaluation	Excellent	Good	General	Poor	Very poor
Appearance/ per	2	7	9	7	5
Filtration effect / per	4	11	10	2	3
Comfort/ per	8	10	8	3	1

the ability of the viral particles to attach and subsequently enter the host cell with the required cell surface receptor interactions; or allow partial mutation of the amino acid sites of the viral surface glycoproteins, which may affect the replication of the viral genome and transcription. Meanwhile, molecular docking studies revealed that *M.bontioides* extracted compounds could associate with SARS-CoV-2 viral proteins and affect the replication and transcription of the virus. Therefore, PAN/*M.bontioides*/Ag-CN/Ag nanofiber membranes showed antiviral activity against H3N2 influenza virus and SARS-CoV-2 coronavirus.

3.9. Application of the PAN/M.bontioides/Ag-CN/Ag nanofibrous membrane.

For the purpose of examining its application in practice, we prepared electrospun fiber mats into masks. As in Fig. 15a, we cut a commercial mask and replaced the filter layer of the commercial mask with an electrospun fiber mat to obtain a photocatalytic mask (Fig. 15b). Our photocatalytic masks had the same facial coverage as the commercial mask, as well as our masks emit *M.bontioides* plant fresh fragrance to reduce adverse reactions and boost comfort (Fig. 15c-d).

The cytocompatibility of the nanofibrous membranes was determined with bone marrow MSCs, and the value-added growth of the cells at 1, 3, and 5 days was observed. Fig. S6 exhibited the growth and proliferation of bone marrow MSCs on the surface of the nanofiber membrane. The ability of bone marrow MSCs to grow and proliferate normally on the surface of the nanofiber membrane as observed by live-dead cell staining indicates the low toxicity of the nanofiber membrane. Meanwhile, the absorbance of the cells was detected by Thermo Science Multiskan GO microplate instrument, and it was found that the number of bone marrow MSCs increased with the increase of culture time. The results indicated that the prepared samples had favorable cytocompatibility and were friendly to human skin.

We randomly asked 30 passersby to evaluate the appearance, filtration effect and comfort of the produced photocatalytic prototype masks. The evaluation was divided into 5 levels and the results were listed in Table 8. The appearance of our handmade masks was still quite different from commercial masks, so most passersby were not very satisfied with them. However, most passersby were pleased and approved of the filtration effect and comfort of the made masks. It demonstrated that PAN/M.bontioides/Ag-CN/Ag nanofiber films were expected to be used in medical masks.

4. Conclusion

In conclusion, this study has demonstrated a multifunctional composite material prepared from plant extracts and Ag-CN photocatalytic material with potential applications in personal protective materials. The electrospinning technology enhances both the filtration and breathability of the mask, in which the nanofibrous membrane produced

has a uniform diameter of 726.93 ± 140.50 nm and strong electrostatic attraction, endowing the mask with superior pathogen filtration capability. The micro-pores formed between the nanofibrous membrane enable excellent breathability and air permeability with an average particle filtration efficiency of 99.82% ± 0.019%. The addition of photocatalyst Ag-CN enables PAN/*M.bontioids*/Ag-CN/Ag nanofiber membranes to be used as photocatalytic bactericidal materials. It not only enables the photocatalytic degradation of pollutants with a 96.37% degradation rate of methylene blue; but also the ROS generated could eliminate pathogens immediately. The bactericidal effects on *E.coli* and *S.aureus* are 98.65 ± 1.49% and 97.8 ± 1.27%, respectively, at 3 h of light exposure. It could reduce secondary infections and environmental pollution caused by discarded masks. The obtained nanofibrous membrane can achieve 3 cycles of sterilization to prolong its life span. Molecular docking revealed that the compounds in *M.bontioides* extracts interacted with neo-coronavirus targets mainly on two proteins, Mpro and RdRp, in which the acteoside exhibited the highest docking energy and the smallest docking radius with the Mpro protein. Moreover, the high number of key amino acid binding sites around the target site of Mpro protein results in a high impact on the replication and transcription process of neo-coronavirus. The PAN/*M.bontioides*/Ag-CN/Ag nanofibrous membrane exerts antiviral activity against the H3N2 virus. Although it was still limited by the long-term illumination to meet the requirements and unsatisfied wearing resistance, we strongly believe that the prepared nanofibrous membranes would act as promising protective materials in the future.

Declaration of Competing Interest

The authors declare that they have no known competing financial interests or personal relationships that could have appeared to influence the work reported in this paper.

Acknowledgements

This work was financially supported by the Science and Technology Foundation of Guangdong Province (2020A0505100050, 2020A1515011004) and special scientific research project of Guangdong universities (2020KZDZX1035), Nanning Local Scientific Research and Technology Development Plan Project (20213122) and Open project of Hunan Provincial Key Laboratory of Environmental Photocatalysis Application Technology (2114502) are gratefully acknowledged.

Appendix A. Supplementary material

Supplementary data to this article can be found online at https://doi.org/10.1016/j.seppur.2022.121565.

References

[1] A. Mingrui Liao, A. Huayang Liu, X.i. Wang, et al., A technical review of face mask wearing in preventing respiratory COVID-19 transmission, Curr. Opin. Colloid In. 52 (2021), 101417.
[2] J. Xu, X. Xiao, W. Zhang, R. Xu, S.C. Kim, Y.i. Cui, T.T. Howard, E. Wu, Y.i. Cui, Air-filtering masks for respiratory protection from PM2.5 and pandemic pathogens, One Earth 3 (5) (2020) 574–589.
[3] L. De Sio, B. Ding, M. Focsan, K. Kogermann, P. Pascoal-Faria, F. Petronela, G. Mitchell, E. Zussman, F. Pierini, Personalized reusable face masks with smart nano-assisted destruction of pathogens for COVID-19: A visionary road, Chem-Eur. J. 27 (20) (2021) 6112–6130.
[4] M. Asif, Y. Xu, F. Xiao, et al., Diagnosis of COVID-19, vitality of emerging technologies and preventive measures, Chem. Eng. J. 423 (2021), 130189.
[5] N.J. Rowan, R.A. Moral, Disposable face masks and reusable face coverings as non-pharmaceutical interventions (NPIs) to prevent transmission of SARS-CoV-2 variants that cause coronavirus disease (COVID-19): Role of new sustainable NPI design innovations and predictive mathematical modelling, Sci. Total Environ. 772 (2021), 145530.
[6] M.A. Chowdhury, M.B.A. Shuvho, M.A. Shahid, et al., Prospect of biobased antiviral face mask to limit the coronavirus outbreak, Environ. Res. 192 (2021), 110294.
[7] R. Saikaew, V. Intasanta, Versatile nanofibrous filters against fine particulates and bioaerosols containing tuberculosis and virus: multifunctions and scalable processing, Separat. Purificat. Technol. 275 (2021) 119171, https://doi.org/10.1016/j.seppur.2021.119171.
[8] L. Meng, F. Hua, Z. Bian, C. Disease, (COVID-19): emerging and future challenges for dental and oral medicine, J. Dent. Res. 99 (2020) (2019) 481–487.
[9] M. Jayaweera, H. Perera, B. Gunawardana, et al., Transmission of COVID-19 virus by droplets and aerosols: a critical review on the unresolved dichotomy, Environ. Res. 188 (2020), 109819.
[10] R. Kouzy, J. Abi Jaoude, A. Kraitem, et al., Coronavirus goes viral: quantifying the COVID-19 misinformation epidemic on twitter, Cureus (2020).
[11] R. Dhand, J. Li, Coughs and sneezes: their role in transmission of respiratory viral infections, including SARS-CoV-2, Am. J. Resp. Crit. Care 202 (2020) 651–659.
[12] S. Dowlath, K. Campbell, F. Al-Barwani, et al., Dry formulation of virus-like particles in electrospun nanofibers, Vaccines 9 (2021) 213.
[13] A. McCarthy, L. Saldana, D.N. Ackerman, Y. Su, J.V. John, S. Chen, S. Weihs, S. P. Reid, J.L. Santarpia, M.A. Carlson, J. Xie, Ultra-absorptive nanofiber swabs for improved collection and test sensitivity of SARS-CoV-2 and other biological specimens, Nano Lett. 21 (3) (2021) 1508–1516.
[14] K.O. Dowd, K.M. Nair, P. Forouzandeh, et al., Face masks and respirators in the fight against the COVID-19 pandemic: a review of current materials, advances and future perspectives, Materials 13 (2020) 3363.
[15] L. Zhang, L. Li, L. Wang, et al., Multilayer electrospun nanofibrous membranes with antibacterial property for air filtration, Appl. Surface Sci. 515 (2020), 145962.
[16] M. Pardo-Figuerez, A. Chiva-Flor, K. Figueroa-Lopez, et al., Antimicrobial nanofiber based filters for high filtration efficiency respirators, Nanomater.-Basel 11 (2021) 900.
[17] M. Qin, D. Liu, X. Meng, et al., Electrospun polyvinyl butyral/berberine membranes for antibacterial air filtration, Mater. Lett.: X 10 (2021), 100074.
[18] Z. Zhang, D. Ji, H. He, et al., Electrospun ultrafine fibers for advanced face masks, Mater. Sci. Eng.: R: Reports 143 (2021), 100594.
[19] W.W.F. Leung, Q. Sun, Electrostatic charged nanofiber filter for filtering airborne novel coronavirus (COVID-19) and nano-aerosols, Separat. Purificat. Technol. 250 (2020), 116886.
[20] D. Qin, R. Zhang, B. Cao, et al., Fabrication of high-performance composite membranes based on hierarchically structured electrospun nanofiber substrates for pervaporation desalination, J. Membrane Sci. 638 (2021), 119672.
[21] Y. Xu, X. Zhang, X. Hao, et al., Micro/nanofibrous nonwovens with high filtration performance and radiative heat dissipation property for personal protective face mask, Chem. Eng. J. 423 (2021), 130175.
[22] W.A. Abbas, B.S. Shaheen, L.G. Ghanem, I.M. Badawy, M.M. Abodouh, S.M. Abdou, S. Zada, N.K. Allam, Cost-effective face mask filter based on hybrid composite nanofibrous layers with high filtration efficiency, Langmuir 37 (24) (2021) 7492–7502.
[23] Y. Cheng, J. Li, M. Chen, et al., Environmentally friendly and antimicrobial bilayer structured fabrics with integrated interception and sterilization for personal protective mask, Separat. Purificat. Technol. 294 (2022), 121165.
[24] H. Ma, B.S. Hsiao, B. Chu, Functionalized electrospun nanofibrous microfiltration membranes for removal of bacteria and viruses, J. Membrane Sci. 452 (2014) 446–452.
[25] H. Khanzada, A. Salam, M.B. Qadir, et al., Fabrication of promising antimicrobial aloe vera/PVA electrospun nanofibers for protective clothing, Materials 13 (2020) 3884.
[26] M. Mariello, A. Qualtieri, G. Mele, M. De Vittorio, Metal-free multilayer hybrid PENG based on soft electrospun/-sprayed membranes with cardanol additive for harvesting energy from surgical face masks, ACS Appl. Mater. Int. 13 (17) (2021) 20606–20621.
[27] N.A. Patil, P.M. Gore, N. Jaya Prakash, et al., Needleless electrospun phytochemicals encapsulated nanofibre based 3-ply biodegradable mask for combating COVID-19 pandemic, Chem. Eng. J. 416 (2021), 129152.
[28] Z.F.M.S. Shohreh Fahimirad, Efficient removal of water bacteria and viruses using electrospun nanofibers, Sci. Total Environ. 751 (2020), 141673.
[29] R. Al-Attabi, J. Rodriguez-Andres, J.A. Schütz, et al., Catalytic electrospun nano-composite membranes for virus capture and remediation, Separat. Purificat. Technol. 229 (2019), 115806.
[30] A.C.C. Bortolassi, S. Nagarajan, B. de Araújo Lima, et al., Efficient nanoparticles removal and bactericidal action of electrospun nanofibers membranes for air filtration, Mater. Sci. Eng.: C 102 (2019) 718–729.
[31] Z. Wang, R. Sahadevan, C. Crandall, et al., Hot-pressed PAN/PVDF hybrid electrospun nanofiber membranes for ultrafiltration, J. Membrane Sci. 611 (2020), 118327.
[32] J.J. Huang, Y. Tian, R. Wang, et al., Fabrication of bead-on-string polyacrylonitrile nanofibrous air filters with superior filtration efficiency and ultralow pressure drop, Separat. Purificat. Technol. 237 (2020), 116377.
[33] M.F. Tabatabaei, S. Hosseinzadeh, H.A. Abbaszadeh, et al., Optimization of topography and surface properties of polyacrylonitrile-based electrospun scaffolds via nonoclay concentrations and its effect on osteogenic differentiation of human mesenchymal stem cells, Iran J. Pharm. Res. 20 (2021) 385–504.
[34] P. Chen, M. Chai, Z. Mai, et al., Electrospinning polyacrylonitrile (PAN) based nanofiberous membranes synergic with plant antibacterial agent and silver nanoparticles (AgNPs) for potential wound dressing, Mater. Today Commun. 31 (2022), 103336.
[35] X. Zhang, R. Lv, L. Chen, R. Sun, Y. Zhang, R. Sheng, T. Du, Y. Li, Y. Qi, A Multifunctional janus electrospun nanofiber dressing with biofluid draining, monitoring, and antibacterial properties for wound healing, ACS Appl. Mater. Inter. 14 (11) (2022) 12984–13000.

[36] L.Z.Y.X. Junke Song, J.W.S.T. Wen Zhang, Q.L.F.L. Liu, et al., The comprehensive study on the therapeutic effects of baicalein for the treatment of COVID-19 in vivo and in vitro, Biochem. Pharmacol. 183 (2020), 114302.

[37] J. Weng, L. Bai, W. Lin, et al., A flavone constituent from myoporum bontioides induces M-phase cell cycle arrest of MCF-7 breast cancer cells, Molecules 22 (2017) 472.

[38] L. Dong, L. Huang, H. Dai, et al., Anti-MRSA sesquiterpenes from the semi-mangrove plant myoporum bontioides A. Gray, Mar. Drugs 16 (2018) 438.

[39] W. Li, P. Xiong, W. Zheng, et al., Identification and antifungal activity of compounds from the mangrove endophytic fungus Aspergillus clavatus R7, Marine Drugs 15 (2017) 259.

[40] M. Kanemoto, K. Matsunami, H. Otsuka, T. Shinzato, C. Ishigaki, Y. Takeda, Chlorine-containing iridoid and iridoid glucoside, and other glucosides from leaves of Myoporum bontioides, Phytochemistry 69 (13) (2008) 2517–2522.

[41] J.C.B.V. Lad Williams, In vitro anti-proliferation/cytotoxic activity of epingaione and its derivatives on the human SH-SY5Y neuroblastoma and TE-671 sarcoma cells, West Ind. Med. J. 56 (2007) 5.

[42] B. Ajitha, C.W. Ahn, P.V.K. Yadav, et al., Silver nanoparticle embedded polymethacrylic acid/ polyvinylpyrrolidone nanofibers for catalytic application, J. Environ. Chem. Eng. 9 (2021), 106291.

[43] B.-H. Mao, Z.-Y. Chen, Y.-J. Wang, S.-J. Yan, Silver nanoparticles have lethal and sublethal adverse effects on development and longevity by inducing ROS-mediated stress responses, Sci Rep-UK 8 (1) (2018), https://doi.org/10.1038/s41598-018-20728-z.

[44] C. Liu, Y. Zhu, X. Lun, H. Sheng, A. Yan, Effects of wound dressing based on the combination of silver@curcumin nanoparticles and electrospun chitosan nanofibers on wound healing, Bioengineered 13 (2) (2022) 4328–4339.

[45] Y. Ju, T. Han, J. Yin, et al., Bumpy structured nanofibrous membrane as a highly efficient air filter with antibacterial and antiviral property, Sci. Total Environ. 777 (2021), 145768.

[46] Y.Z.L.K. Jiao Wang, P.L.W.S. Li, Zhang, Low-voltage driven Ag-Co_3O_4 textile device for multifunctional air cleaning, Chem. Eng. J. 424 (2021), 130320.

[47] Y.O. Ayipo, A.A. Bakare, U.M. Badeggi, et al., Recent advances on therapeutic potentials of gold and silver nanobiomaterials for human viral diseases, Curr. Res. Chem. Biol. 2 (2022), 100021.

[48] D.H. Park, Y.H. Joe, A. Piri, et al., Determination of air filter anti-viral efficiency against an airborne infectious virus, J. Hazard. Mater. 396 (2020), 122640.

[49] C. Tian, F. Wu, W. Jiao, et al., Antibacterial and antiviral N-halamine nanofibrous membranes with nanonet structure for bioprotective applications, Compos. Commun. 24 (2021), 100668.

[50] A. Eka Putri, L. Roza, S. Budi, et al., Tuning the photocatalytic activity of nanocomposite ZnO nanorods by shape-controlling the bimetallic AuAg nanoparticles, Appl. Surface Sci. 536 (2021), 147847.

[51] N.A.F. Al-Rawashdeh, O. Allabadi, M.T. Aljarrah, Photocatalytic activity of graphene oxide/zinc oxide nanocomposites with embedded metal nanoparticles for the degradation of organic dyes, ACS Omega 5 (43) (2020) 28046–28055.

[52] S. Karagoz, N.B. Kiremitler, G. Sarp, S. Pekdemir, S. Salem, A.G. Goksu, M.S. Onses, I. Sozdutmaz, E. Sahmetlioglu, E.S. Ozkara, A. Ceylan, E. Yilmaz, Antibacterial, antiviral, and self-cleaning mats with sensing capabilities based on electrospun nanofibers decorated with ZnO nanorods and ag nanoparticles for protective clothing applications, ACS Appl. Mater. Int. 13 (4) (2021) 5678–5690.

[53] X. Zeng, S. Lan, I.M.C. Lo, Rapid disinfection of E. coli by ternary $BiVO_4$/Ag/g-C_3N_4 composite under visible light: photocatalysis mechanism and performance investigation in authentic sewage, Environ. Sci. Nano 6 (2019) 610–623.

[54] Y. Tong, G. Shi, G. Hu, et al., Photo-catalyzed TiO_2 inactivates pathogenic viruses by attacking viral genome, Chem. Eng. J. 414 (2021), 128788.

[55] X.L.X.L. Ran Tao, Discrete heterojunction nanofibers of $BiFeO_3$/Bi_2WO_6: Novel architecture for effective charge separation and enhanced photocatalytic performance, J. Colloid Interf. Sci. (2020) 257–268.

[56] M. Humayun, H. Ullah, L. Shu, X. Ao, A.A. Tahir, C. Wang, W. Luo, Plasmon Assisted highly efficient visible light catalytic CO_2 reduction over the noble metal decorated Sr-incorporated g-C_3N_4, Nano-Micro Lett 13 (1) (2021), https://doi.org/10.1007/s40820-021-00736-x.

[57] J. Huang, D. Li, R. Li, Q. Zhang, T. Chen, H. Liu, Y. Liu, W. Lv, G. Liu, An efficient metal-free phosphorus and oxygen co-doped g-C_3N_4 photocatalyst with enhanced visible light photocatalytic activity for the degradation of fluoroquinolone antibiotics, Chem. Eng. J. 374 (2019) 242–253.

[58] W. Oh, L. Lok, A. Veksha, et al., Enhanced photocatalytic degradation of bisphenol A with Ag-decorated S-doped g-C_3N_4 under solar irradiation: performance and mechanistic studies, Chem. Eng. J. 333 (2018) 739–749.

[59] M. Ramachandra, S. Devi Kalathiparambil Rajendra Pai, J. Resnik Jaleel UC, et al., Improved photocatalytic activity of g-C_3N_4/ZnO: a potential direct Z-scheme nanocomposite, Chemistryselect 5 (2020) 11986-11995.

[60] R. Zhang, Y. Ma, W. Lan, et al., Enhanced photocatalytic degradation of organic dyes by ultrasonic-assisted electrospray TiO_2/graphene oxide on polyacrylonitrile/β-cyclodextrin nanofibrous membranes, Ultrasonics Sonochemistry 70 (2021), 105343.

[61] S.J.V.J. Akshara, P. Shah, High performance visible light photocatalysis of electrospun PAN/ZnO hybrid nanofibers, J. Ind. Eng. Chem. (2019).

[62] Q. Li, Y. Yin, D. Cao, Y. Wang, P. Luan, X. Sun, W. Liang, H. Zhu, Photocatalytic rejuvenation enabled self-sanitizing, reusable, and biodegradable masks against COVID-19, ACS Nano 15 (7) (2021) 11992–12005.

[63] W. Lu, C. Chen, C. Cho, et al., Antibacterial activity and protection efficiency of polyvinyl butyral nanofibrous membrane containing thymol prepared through vertical electrospinning, Polymers-Basel 13 (2021) 1122.

[64] A. Roy, O. Bulut, S. Some, et al., Green synthesis of silver nanoparticles: biomolecule-nanoparticle organizations targeting antimicrobial activity, RSC Adv. 9 (2019) 2673–2702.

[65] M.K. Haider, A. Ullah, M.N. Sarwar, et al., Fabricating antibacterial and antioxidant electrospun hydrophilic polyacrylonitrile nanofibers loaded with AgNPs by lignin-induced in-situ method, Polymers-BASEL 13 (2021) 748.

[66] R. Al-Attabi, Y. Morsi, W. Kujawski, L. Kong, J.A. Schütz, L.F. Dumée, Wrinkled silica doped electrospun nano-fiber membranes with engineered roughness for advanced aerosol air filtration, Separat. Purificat. Technol. 215 (2019) 500–507.

[67] S. Zheng, H. Chen, X. Tong, et al., Integration of a photo-fenton reaction and a membrane filtration using CS/PAN@FeOOH/g-C_3N_4 electrospun nanofibers: synthesis, characterization, self-cleaning performance and mechanism, Appl. Catal. B: Environ. 281 (2021), 119519.

[68] A. Adamczak, M. Ożarowski, T.M. Karpiński, Antibacterial activity of some flavonoids and organic acids widely distributed in plants, J. Clin. Med. 9 (2020) 109.

[69] A.B. Pradhan, S. Bhuiya, L. Haque, S. Das, Role of hydroxyl groups in the B-ring of flavonoids in stabilization of the Hoogsteen paired third strand of Poly(U).Poly(A)* Poly(U) triplex, Arch. Biochem. Biophys. 637 (2018) 9–20.

[70] R. Sankaranarayanan, C. Valiveti, D. Kumar, et al., The flavonoid metabolite 2,4,6-trihydroxybenzoic acid is a CDK inhibitor and an anti-proliferative agent: a potential role in cancer prevention, Cancers 11 (2019) 427.

[71] C. Bai, Q. Zhong, G.F. Gao, Overview of SARS-CoV-2 genome-encoded proteins, Sci. China Life Sci. 65 (2) (2022) 280–294.

[72] C. Baruah, P. Devi, D.K. Sharma, Sequence Analysis and structure prediction of SARS-CoV-2 accessory proteins 9b and ORF14: evolutionary analysis indicates close relatedness to bat coronavirus, Biomed Res. Int. 2020 (2020) 1–13.

[73] B. Boson, V. Legros, B. Zhou, et al., The SARS-CoV-2 envelope and membrane proteins modulate maturation and retention of the spike protein, allowing assembly of virus-like particles, J. Biol. Chem. 296 (2021), 100111.

[74] S. Satarker, M. Nampoothiri, Structural proteins in severe acute respiratory syndrome coronavirus-2, Arch. Med. Res. 51 (6) (2020) 482–491.

[75] D. Choi, M. Choi, H. Jeong, et al., Co-existing "spear-and-shield" air filter: Anchoring proteinaceous pathogen and self-sterilized nanocoating for combating viral pandemic, Chem. Eng. J. 426 (2021), 130763.

[76] N.A. Murugan, C.J. Pandian, J. Jeyakanthan, Computational investigation on Andrographis paniculata phytochemicals to evaluate their potency against SARS-CoV-2 in comparison to known antiviral compounds in drug trials, J. Biomol. Struct. Dyn. 39 (12) (2021) 4415–4426.

[77] R. Alexpandi, J.F. De Mesquita, S.K. Pandian, A.V. Ravi, Quinolines-based SARS-CoV-2 3CLpro and RdRp inhibitors and spike-RBD-ACE2 inhibitor for drug-repurposing against COVID-19: an in silico analysis, Front. Microbiol. 11 (2020).

[78] Z. Jin, X. Du, Y. Xu, Y. Deng, M. Liu, Y. Zhao, B. Zhang, X. Li, L. Zhang, C. Peng, Y. Duan, J. Yu, L. Wang, K. Yang, F. Liu, R. Jiang, X. Yang, T. You, X. Liu, X. Yang, F. Bai, H. Liu, X. Liu, L.W. Guddat, W. Xu, G. Xiao, C. Qin, Z. Shi, H. Jiang, Z. Rao, H. Yang, Structure of Mpro from SARS-CoV-2 and discovery of its inhibitors, Nature 582 (7811) (2020) 289–293.

[79] A. Rosell-Hidalgo, L. Young, A.L. Moore, et al., QSAR and molecular docking for the search of AOX inhibitors: a rational drug discovery approach, J. Comput. Aid. Mol. Des. 35 (2021) 245–260.

[80] X. Fu, T. Belwal, Y. He, et al., Interaction and binding mechanism of cyanidin-3-O-glucoside to ovalbumin in varying pH conditions: a spectroscopic and molecular docking study, Food Chem. 320 (2020), 126616.

[81] Y. Masoudi-Sobhanzadeh, B. Jafari, S. Parvizpour, et al., A novel multi-objective metaheuristic algorithm for protein-peptide docking and benchmarking on the LEADS-PEP dataset, Comput. Biol. Med. 138 (2021), 104896.